



# MIT Open Access Articles

## *Spitzer Variability Properties of Low-gravity L Dwarfs*

The MIT Faculty has made this article openly available. **Please share** how this access benefits you. Your story matters.

<b>As Published</b>	10.3847/1538-3881/AB9642
<b>Publisher</b>	American Astronomical Society
<b>Version</b>	Final published version
<b>Citable link</b>	<a href="https://hdl.handle.net/1721.1/132407">https://hdl.handle.net/1721.1/132407</a>
<b>Terms of Use</b>	Article is made available in accordance with the publisher's policy and may be subject to US copyright law. Please refer to the publisher's site for terms of use.



# Spitzer Variability Properties of Low-gravity L Dwarfs

Johanna M. Vos<sup>1</sup>, Beth A. Biller<sup>2,3</sup>, Katelyn N. Allers<sup>4</sup>, Jacqueline K. Faherty<sup>1</sup>, Michael C. Liu<sup>5</sup>, Stanimir Metchev<sup>6</sup>, Simon Eriksson<sup>7</sup>, Elena Manjavacas<sup>8</sup>, Trent J. Dupuy<sup>9</sup>, Markus Janson<sup>7</sup>, Jacqueline Radigan-Hoffman<sup>10</sup>, Ian Crossfield<sup>11</sup>, Mickaël Bonnefoy<sup>12</sup>, William M. J. Best<sup>13</sup>, Derek Homeier<sup>14</sup>, Joshua E. Schlieder<sup>15</sup>, Wolfgang Brandner<sup>16</sup>, Thomas Henning<sup>16</sup>, Mariangela Bonavita<sup>2,3</sup>, and Esther Buenzli<sup>17</sup>

<sup>1</sup> Department of Astrophysics, American Museum of Natural History, Central Park West at 79th Street, New York, NY 10024, USA; [jvos@amnh.org](mailto:jvos@amnh.org)

<sup>2</sup> SUPA, Institute for Astronomy, University of Edinburgh, Blackford Hill, Edinburgh EH9 3HJ, UK

<sup>3</sup> Centre for Exoplanet Science, University of Edinburgh, Edinburgh, UK

<sup>4</sup> Department of Physics and Astronomy, Bucknell University, Lewisburg, PA 17837, USA

<sup>5</sup> Institute for Astronomy, University of Hawaii at Manoa, Honolulu, HI 96822, USA

<sup>6</sup> Department of Physics & Astronomy and Centre for Planetary Science and Exploration, The University of Western Ontario, London, Ontario N6A 3K7, Canada

<sup>7</sup> Department of Astronomy, Stockholm University, AlbaNova University Center, SE-106 91 Stockholm, Sweden

<sup>8</sup> W.M. Keck Observatory, 65-1120 Mamalahoa Highway, Kamuela, HI 96743, USA

<sup>9</sup> Gemini Observatory, Northern Operations Center, 670 N. A'ohoku Place, Hilo, HI 96720, USA

<sup>10</sup> Utah Valley University, 800 West University Parkway, Orem, UT 84058, USA

<sup>11</sup> Physics & Astronomy Department, University of Kansas, Lawrence, KS, USA

<sup>12</sup> Univ. Grenoble Alpes, IPAG; CNRS, IPAG, F-38000 Grenoble, France

<sup>13</sup> The University of Texas at Austin, Department of Astronomy, 2515 Speedway C1400, Austin, TX 78712, USA

<sup>14</sup> Zentrum für Astronomie der Universität Heidelberg, Landessternwarte, Königstuhl 12, D-69117 Heidelberg, Germany

<sup>15</sup> Exoplanets and Stellar Astrophysics Laboratory, Code 667, NASA Goddard Space Flight Center, Greenbelt, MD 20771, USA

<sup>16</sup> Max-Planck-Institut für Astronomie, Königstuhl 17, D-69117 Heidelberg, Germany

<sup>17</sup> Institute for Particle Physics and Astrophysics, ETH Zurich, Wolfgang-Pauli-Strasse 27, 8093, Zurich, Switzerland

Received 2020 February 26; revised 2020 May 21; accepted 2020 May 21; published 2020 June 24

## Abstract

We present Spitzer Space Telescope variability monitoring observations of three low-gravity L dwarfs with previous detections of variability in the near-IR: 2MASS J0045+16, 2MASS J0501–00, and 2MASS J1425–36. We detect significant periodic variability in two of our targets, 2MASS J0045+16 and 2MASS J0501–00. We do not detect variability in 2MASS J1425–36. Combining our new rotation periods with rotational velocities, we calculate inclination angles of  $22^\circ \pm 1^\circ$ ,  $60_{-8}^{+13^\circ}$ , and  $52_{-13}^{+19^\circ}$  for 2MASS J0045+16, 2MASS J0501–00, and 2MASS J1425–36, respectively. Our three new objects are consistent with the tentative relations between inclination, amplitude, and color anomaly previously reported. Objects with the highest variability amplitudes are inclined equator on, while the maximum observed amplitude decreases as the inclination angle decreases. We also find a correlation between the inclination angle and  $(J - K)_{2MASS}$  color anomaly for the sample of objects with measured inclinations. Compiling the entire sample of brown dwarfs with Spitzer variability detections, we find no enhancement in amplitude for young, early-L dwarfs compared to the field dwarf population. We find a possible enhancement in amplitude of low-gravity late-L dwarfs at  $4.5 \mu\text{m}$ . We do not find a correlation between amplitude ratio and spectral type for field dwarfs or for the young population. Finally, we compile the rotation periods of a large sample of brown dwarfs with ages 1 Myr–1 Gyr and compare the rotation rates predicted by evolutionary models assuming angular momentum conservation. We find that the rotation rates of the current sample of brown dwarfs fall within the expected range set by evolutionary models and breakup limits.

*Unified Astronomy Thesaurus concepts:* Brown dwarfs (185); L dwarfs (894); Atmospheric variability (2119)

*Supporting material:* machine-readable table

## 1. Introduction

Photometric variability monitoring directly probes atmospheric features in exoplanet and brown dwarf atmospheres, as it is sensitive to the spatial distribution of inhomogeneities such as condensate clouds, and compositional and/or temperature fluctuations (Marley et al. 2012; Tremblin et al. 2016) as a planet rotates. Variability studies of field brown dwarfs have begun to reveal the complex, evolving nature of their atmospheres (Biller 2017; Artigau 2018, and references therein). Recent variability monitoring with Spitzer and the Very Large Array has provided the first direct measurements of the wind speed on a brown dwarf, finding a strong eastward wind of  $\sim 650 \text{ m s}^{-1}$  for the cool T dwarf 2MASS J10475385+2124234 (Allers et al. 2020). For the majority of directly imaged planets, however, the contrast between host star and planet makes it difficult to obtain sufficiently high signal-to-noise ratio

photometry to allow precise variability monitoring (Apari et al. 2016). Young, free-floating brown dwarfs provide an excellent analog to directly imaged planets. They share remarkably similar masses, radii, and spectra to the directly imaged planets (Liu et al. 2013, 2016; Faherty et al. 2016) and can be observed in detail with current facilities.

In recent years, variability studies of the low-gravity exoplanet analogs have revealed important insights into their atmospheres. Metchev et al. (2015) noted a tentative correlation between low gravity and high-amplitude variability in a sample of six mid-L-type brown dwarfs as part of a larger Spitzer variability survey. A number of high-amplitude variability detections have since been reported in free-floating planetary-mass objects (Biller et al. 2015; Lew et al. 2016; Schneider et al. 2018; Vos et al. 2018) and wide, low-gravity companions (Zhou et al. 2016, 2019, 2020; Bowler et al. 2020).

In Vos et al. (2019), we carried out a large, ground-based,  $J$ -band survey for variability in isolated low-mass brown dwarfs, finding a 30% variability fraction among low-gravity L dwarfs, compared to 11% for the higher-gravity, field brown dwarf population surveyed by Radigan et al. (2014). This may be a result of the high-altitude clouds found in low-gravity atmospheres (Marley et al. 2012) providing a higher contrast ratio between cloud layers which would enhance the amplitude produced by inhomogeneities in the cloud deck.

As part of a large survey for  $J$ -band variability in low-mass brown dwarfs with NTT/SofI, we detected variability in six young L-type dwarfs (Vos et al. 2019). We have carried out follow-up monitoring of two detections, the late-L objects PSO J318.533822.8603 (PSO 318.5-22) and 2MASS J2244316+204343 (2M2244+20) in previous Spitzer cycles (Biller et al. 2018; Vos et al. 2018) and here we present follow-up mid-IR monitoring of the three L2–L5 spectral-type detections from this survey: 2MASS J00452143+1634446 (hereafter 2MASS J0045+16), 2MASS J05012406–0010452 (hereafter 2MASS J0501–00), and 2MASS J14252798–3650229 (hereafter 2MASS J1425–36).

All three objects show robust evidence of youth and/or low gravity. The L2 object 2MASS J0045+16 is a confirmed member of the 50 Myr old Argus association (Faherty et al. 2016; Liu et al. 2016) and shows signs of very low gravity in its spectrum (Allers & Liu 2013; Gagné et al. 2015). Riedel et al. (2019) find that the kinematics of 2MASS J0045+16 may be consistent with the younger 23 Myr  $\beta$  Pictoris moving group using their LACEwING group membership code (Riedel et al. 2017). The L3 object 2MASS J0501–00 is not associated with a known young moving group but shows signs of very low gravity in its optical and IR spectra (Cruz et al. 2009; Allers & Liu 2013). Both Liu et al. (2016) and Faherty et al. (2016) classify 2MASS J0501–00 as a young field object. The L4 object 2MASS J1425–36 is a member of the 110–150 Myr old AB Doradus moving group (Faherty et al. 2016; Liu et al. 2016) and has been classified as an intermediate-gravity object based on its IR spectrum (Gagné et al. 2015). All three targets have estimated evolutionary model masses of 20–25  $M_{\text{Jup}}$  based on their bolometric luminosities (Faherty et al. 2016).

In addition, we obtained Gemini/GNIRS high-resolution spectra of 2MASS J0501–00 and re-reduced Keck/NIRSPEC spectra for 2MASS J0045+16 and 2MASS J0501–00. In Section 2, we describe the analysis of our high-resolution spectra, in Section 3, we describe the Spitzer observations and data reduction, in Section 4, we describe how we identified variables, and in Sections 7–9, we describe our results in the context of brown dwarf variability amplitudes, inclination angles, and rotation periods.

## 2. Target Rotational Velocities and Maximum Periods

2MASS J0045+16 and 2MASS J1425–36 have high-resolution NIRSPEC-7 data from Keck/NIRSPEC in the Keck Observatory Archive (Program IDs C34NS and N58NS; PI: Charbonneau). We additionally obtained a high-dispersion spectrum of 2MASS J0501–00 using Gemini/GNIRS (PID: GN-2017B-Q-58). We used the 111 line  $\text{mm}^{-1}$  grating and the long camera ( $0''.05$  per pixel) with a  $0''.10$  slit, centered at  $2.3 \mu\text{m}$ . We obtained four 600 s exposures taken in an ABBA nod pattern. The data were reduced using a modified version of the REDSPEC package as described in Vos et al. (2017).

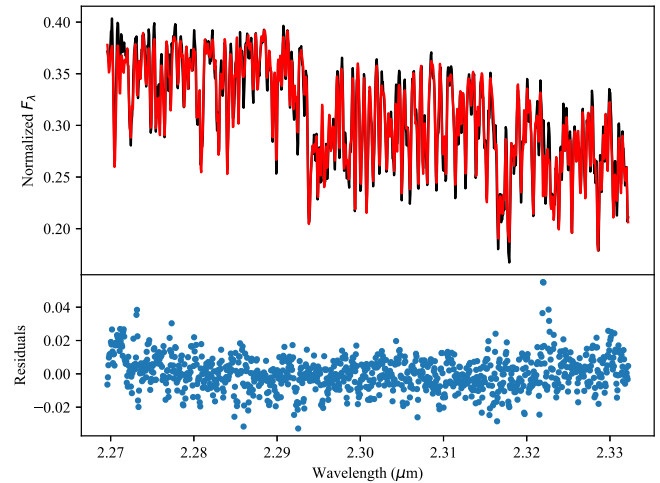


**Figure 1.** Top panel: Gemini/GNIRS spectrum of 2MASS J0501–00 shown in black, with our best-fit model overplotted in red. Bottom panel: residuals of the fit.

We use the method outlined in our previous work (Allers et al. 2016; Vos et al. 2017) to calculate the radial and rotational velocity of our three targets. We use forward modeling to simultaneously fit the wavelength solution, the scaling of telluric line depths, the FWHM of the instrument line-spread function, and the target radial and rotation velocities. The BT-Settl model atmospheres (Allard et al. 2012) are used as the intrinsic spectrum for each target. We use Markov Chain Monte Carlo (MCMC) methods to determine the posterior distributions for our forward-model parameters. To ensure that the median absolute residual of the fit agrees with the median uncertainty of our spectra, we include a systematic uncertainty in our analysis. We obtain a systematic uncertainty of 1.9% for 2MASS J0045+16, 1.7% for 2MASS J0501–00, and 3% for 2MASS J1425–36. Radial velocity (RV) and  $v \sin(i)$  values and their  $1\sigma$  uncertainties are determined from their marginalized distributions obtained from our MCMC method. For more details on the method, we refer the reader to Allers et al. (2016). In Figure 1, we show the observed spectrum of 2MASS J0501–00, our fit to the data, and the residuals of the fit. We show our measured  $v \sin(i)$  and RV values for all three targets in Table 1.

Blake et al. (2010) have previously reported  $v \sin(i)$  values for 2MASS J0045+16 and 2MASS J1425–36. For 2MASS J0045+16, they report a value of  $32.82 \pm 0.17 \text{ km s}^{-1}$ , which is within  $3\sigma$  of our value. Our obtained uncertainty ( $\sim 0.4 \text{ km s}^{-1}$ ) is significantly larger than the reported uncertainty of  $\sim 0.17 \text{ km s}^{-1}$  in Blake et al. (2010). For 2MASS J1425–36, they report a  $v \sin(i)$  value of  $32.37 \pm 0.66 \text{ km s}^{-1}$ , which is within  $2\sigma$  of our value. Our obtained uncertainties for 2MASS J1425–36 are similar to the reported uncertainties from Blake et al. (2010). No previous  $v \sin(i)$  values have been reported for 2MASS J0501–00.

By combining our measured  $v \sin(i)$  values with a radius estimate (Filippazzo et al. 2015), we determine the maximum rotation period for each of our three targets. We find that the maximum rotation period for 2MASS J0045+16, 2MASS J0501–00, and 2MASS J1425–36 are  $\sim 6.4$  hr, 19.6 hr, and 5.6 hr, respectively. In order to accurately constrain the rotation period of each of our targets, we chose an observation duration twice that of each object’s maximum rotation period for our Spitzer variability monitoring observations.

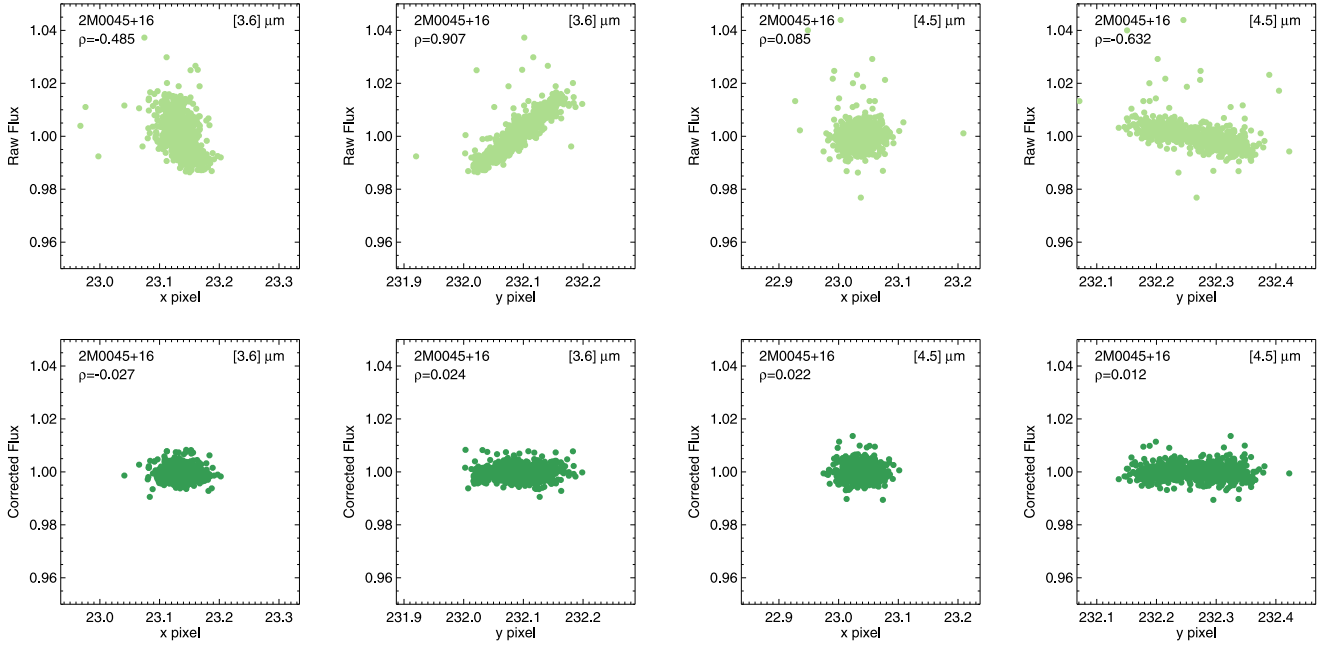


**Figure 2.** Raw Spitzer/IRAC photometry obtained from aperture photometry is highly correlated with  $x$  and  $y$  subpixel positions. We correct for this by fitting a cubic function. Top panels show the correlation between the raw flux and pixel position. Bottom panels show the corrected flux plotted against pixel position. Spearman’s  $\rho$  coefficient is a measure of the significance of correlation between two values—in all cases, Spearman’s  $\rho$  coefficient decreases after pixel-phase correction.

**Table 1**  
Measured  $v \sin(i)$  values, Rotation Periods, and Inclinations for 2MASS J0045+16, 2MASS J0501–00, and 2MASS J1425–36

Target	$v \sin(i)$ (km s <sup>−1</sup> )	RV (km s <sup>−1</sup> )	Period (hr)	Radius Estimate	Inclination
2MASS J0045+16	$31.76^{+0.45}_{-0.41}$	$5.19^{+0.22}_{-0.25}$	$2.4 \pm 0.1$	$1.62 \pm 0.06$	$22^\circ \pm 1^\circ$
2MASS J0501–00	$9.57^{+0.67}_{-0.58}$	$24.65^{+0.14}_{-0.17}$	$15.7 \pm 0.2$	$1.38 \pm 0.18$	$60^{+20^\circ}_{-9^\circ}$
2MASS J1425–36	$33.08^{+0.53}_{-0.49}$	$5.38 \pm 0.27$	$2.5\text{--}5.6$	$1.32 \pm 0.09$	$54^{+36^\circ}_{-15^\circ}$

### 3. Spitzer Observations and Data Reduction

We used the Infrared Array Camera (IRAC; Fazio et al. 2004) to observe our targets in the Channel 1 (3.6  $\mu\text{m}$ ) and Channel 2 (4.5  $\mu\text{m}$ ) bands as part of the Cycle 14 Program, “Weather and Rotation of Young Brown Dwarfs” (PID: 14019). We observed each target for twice their rotation period in both bands, resulting in a total observation duration of 12.8 hr, 39.2 hr, and 11.2 hr for 2MASS J0045+16, 2MASS J0501–00, and 2MASS J1425–36, respectively. The observations were designed following the recommendations for obtaining high-precision photometry from the Spitzer Science Center. Science observations were preceded by a 30 minute dithered sequence to remove the initial slew settling that occurs when acquiring a new target, and followed by a 10 minute dithered sequence. The target was placed on the well-characterized “sweet spot” of the detector for science exposures to minimize correlated noise.

Photometry was obtained from the Basic Calibrated Data images produced by the Spitzer Science Center using pipeline version S19.2. The BOX\_CENTROIDER.PRO routine was used to find the centroids of the target and reference stars of similar brightness in the field of view. Aperture photometry was performed on the target and reference stars using apertures with radii of 2.0–4.0 pixels, in steps of 0.2. We choose the final aperture size that produces the lowest rms target light curve. Outliers were identified and rejected from the raw light curves using a 6 $\sigma$  clip.

Spitzer/IRAC photometry is known to exhibit a systematic effect due to intrapixel sensitivity variations, known as the pixel-phase effect. The top panels in Figure 2 show that the raw photometry is highly correlated with the  $x$  and  $y$  subpixel coordinates. We quantify the strength of correlation by calculating Spearman’s  $\rho$  coefficient (Press et al. 1986). We model the pixel-phase effect as a function of the  $x$  and  $y$  coordinates, and find that linear and quadratic fits do not correct the observed correlation. We model the pixel-phase effect using a cubic function of the  $x$  and  $y$  coordinates (Knutson et al. 2008; Heinze et al. 2015):

$$f(x, y) = P_0 + P_1x + P_2y + P_3xy + P_4x^2 + P_5y^2 + P_6x^3 + P_7y^3 + P_8x^2y + P_9xy^2, \quad (1)$$

where  $f(x, y)$  represents the measured flux,  $p_i$  are the fitted coefficients, and  $x$  and  $y$  are the subpixel coordinates. We correct the light curves of the target and reference stars using Equation (1) and find that the fitted coefficients  $p_i$  are similar for the target and reference stars. We find that this correction decreases the correlation between the flux and pixel position for each observation (Figure 2 for 2MASS J0045+16). We present the final corrected light curves in the top panels of Figures 3–5. We additionally show how the  $x$ - and  $y$ -pixel positions vary during each observation in the figures in Appendix B. The variation in pixel position does not correlate with the corrected flux of our variable and nonvariable targets.



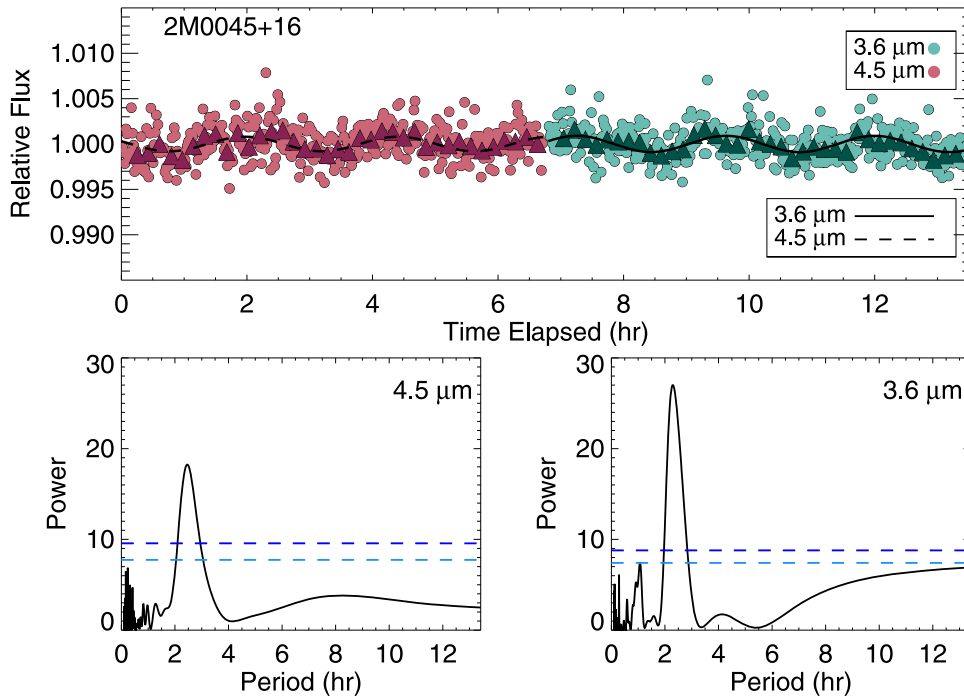


**Figure 3.** Top panel: full corrected Spitzer light curve of 2MASS J0045+16.  $3.6\ \mu\text{m}$  data is shown in green, and the  $4.5\ \mu\text{m}$  is shown in pink. Circles show 30 s cadence and triangles show 10 minute cadence. Best-fit sinusoidal models from our MCMC analysis for each channel are overplotted in black. Bottom panels: periodograms for each observation. The target periodogram is shown in black, reference star periodograms are shown in gray, and the 95% and 99% significance thresholds are shown by the blue dashed lines. The periodogram of 2MASS J0045+16 peaks well above the significance thresholds in both wavelengths. A sinusoidal model fit to both light curves favors a period of  $2.4 \pm 0.1$  hr.

#### 4. Identification of Variables

We search for variability in our observed light curves using the periodogram analysis outlined in Vos et al. (2018) and using a Bayesian framework outlined in Naud et al. (2017).

##### 4.1. Variability Detection with Periodogram Analysis

We calculate the Lomb–Scargle periodograms of our target and reference starlight curves (Scargle 1982) to assess the significance of their trends. For each observation, we calculate the 95% and 99% significance thresholds by simulating 1000 light curves from our observed reference stars. We create the simulated light curves by randomly rearranging the indices of the reference starlight curves, which produces simulated light curves with Gaussian noise equal to that of our observed light curves. The 95% and 99% significance thresholds are plotted in blue in the bottom panels of Figures 3–5. The periodograms of targets 2MASS J0045+16 and 2MASS J0501–00 (Figures 3 and 4) display power that is significantly above the threshold at both  $3.6$  and  $4.5\ \mu\text{m}$ . The periodograms for each target peak at roughly the same period in both channels, which further supports the notion that the variation is rotationally modulated. Our final target, 2MASS J1425–36, shown in Figure 5, does not exhibit periodogram power at the thresholds.

The periodogram analysis in Figure 5 confirms that 2MASS J1425–36 does not exhibit significant variability in either channel. The sensitivity of our Spitzer observations and our knowledge of the maximum period for this target (5.6 hr; Section 2) allow us to place strong constraints on the upper limit of the variability amplitude at each wavelength. To determine these upper limits, we create a sensitivity plot, which shows the variability amplitudes and rotation periods detectable by each observation. We inject sinusoidal curves into light

curves with Gaussian-distributed noise similar to that of 2MASS J1425–36. The simulated light curves have amplitudes of 0.05%–0.5%, rotation periods of 0.5–6 hr, and random phase shifts. We analyze these simulated light curves using the periodogram analysis discussed above and calculate the detection probability as the percentage of light curves with a given variability amplitude and period that produces a periodogram power above the significance threshold. We show these sensitivity plots in Figure 6. Adopting a detection probability of 90% as our threshold, we place upper limits of 0.16% and 0.18% on the  $3.6\ \mu\text{m}$  and  $4.5\ \mu\text{m}$  variability amplitudes, respectively.

Estimating the significance of variability using periodogram analysis assumes that the noise properties of the target and reference stars are the same. This may not be the case if the reference stars are significantly brighter or fainter than the target. The observations of 2MASS J0501–00 include a number of reference stars with similar brightness; however, 2MASS J0045+16 and 2MASS J1425–36 are brighter than their reference stars by  $\Delta\text{mag} \sim 1$ –2. The method also assumes that white noise is the only noise contribution. Reference stars with obvious variability are identified by eye and removed, but there may be residual time-correlated noise in the target and reference stars if the systematics were not adequately removed by Equation (1). If this is the case, the significance thresholds may be slightly underestimated. As none of the reference star periodograms in Figures 3–5 peak above the estimated significance thresholds and none of the reference star periodograms peak at periods similar to the periods of our variable targets, it is likely that the contributions from nonwhite noise do not affect our ability to identify variability using the Lomb–Scargle periodogram. Additionally, because periodic variability is independently recovered in both

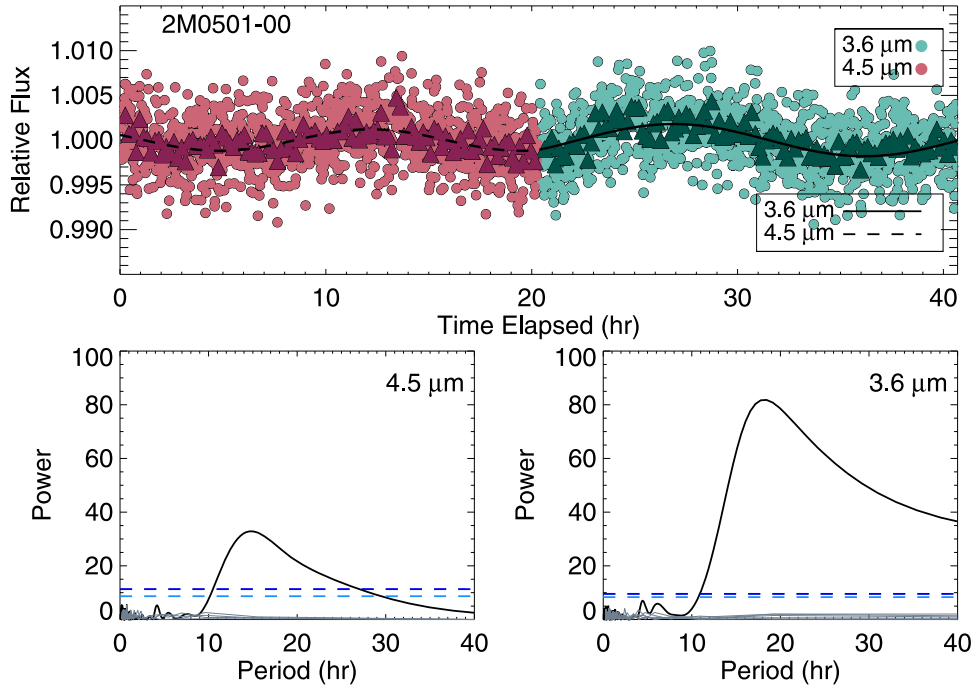


**Figure 4.** Top panel: full corrected Spitzer light curve of 2MASS J0501–00. The  $3.6\ \mu\text{m}$  data are shown in green and  $4.5\ \mu\text{m}$  data are shown in pink. Circles show 30 s cadence and triangles show 10 minute cadence. Best-fit sinusoidal models from our MCMC analysis for each channel are overplotted in black. Bottom panels: periodograms for each observation. The target periodogram is shown in black, reference star periodograms are shown in gray, and the 95% and 99% significance thresholds are shown by the blue dashed lines. The periodogram of 2MASS J0501–00 peaks well above the significance thresholds in both wavelengths. We fit a sinusoidal model to the full light curve, which favors a rotation period of  $15.7 \pm 0.2$  hr.

channels for 2MASS J0045+16 and 2MASS J0501–00, it is likely that the variability is astrophysical in nature.

#### 4.2. Variability Detection Using the Bayesian Information Criterion

We additionally use the Bayesian Information Criterion (BIC) to search for variability in each observation, following the method described in Naud et al. (2017). The BIC is defined as

$$\text{BIC} = -2 \ln \mathcal{L}_{\text{max}} + k \ln N, \quad (2)$$

where  $\mathcal{L}_{\text{max}}$  is the maximum likelihood achievable by the model,  $k$  is the number of parameters in the model, and  $N$  is the number of data points used in the fit (Schwarz 1978).

For each observation, we calculate  $\Delta\text{BIC} = \text{BIC}_{\text{sin}} - \text{BIC}_{\text{flat}}$  to assess whether the variable sinusoidal or nonvariable flat model is favored by the data. The BIC penalizes the sinusoidal model for having additional parameters compared with the flat model. These values are shown in Table 2. A negative value of  $\Delta\text{BIC}$  indicates that the sinusoidal model is favored, and a positive value indicates that the nonvariable, flat model is favored. A  $|\Delta\text{BIC}|$  value between 0 and 6 indicates that one model is positively favored over the other, a value between 6 and 10 indicates that one model is strongly favored over the other, and values above 10 indicate that one model is very strongly favored over the other (Schwarz 1978). All of the  $|\Delta\text{BIC}|$  values shown in Table 2 are much greater than 10, showing that these results are highly significant. A variable, sinusoidal model is very strongly preferred for 2MASS J0045+16 and 2MASS J0501–00, while a nonvariable, flat model is very strongly favored for 2MASS J1425–36. These results are fully consistent with the periodogram method for identifying variability discussed in Section 4.

#### 4.3. Determining Rotation Periods Using MCMC

To determine the rotation period and variability amplitude of our variable objects, we use the MCMC algorithm EMCEE (Foreman-Mackey et al. 2013) to fit a sinusoidal model to the data in each band for 2MASS J0045+16 and 2MASS J0501–00. Both variable objects exhibit fairly uniform, sinusoidal light curves and thus do not warrant a Fourier model fit with additional parameters (e.g., Vos et al. 2018). For the MCMC analysis, we use 1000 walkers with 10,000 steps. We discard the initial 1000 steps as the burn-in sample. We check for convergence by visually inspecting the resulting chains for each parameter to check that they are consistent with random noise of constant mean and variance. We also check that there is no difference between the parameter constraints obtained from the first and second halves of the chain. Based on these two checks, we find that the MCMC converges well for each sinusoidal model fit.

We show the final posterior distributions of the variability amplitude, rotation period, and phase in Figures A1 and A2 of Appendix A, and present the best-fit parameters and their  $1\sigma$  errors in Table 2. We overplot the best-fit sinusoidal model for each channel in Figures 3 and 4. The residuals of the fit are normally distributed. For 2MASS J0045+16, the measured rotation periods of  $2.37^{+0.08}_{-0.06}$  hr at  $3.6\ \mu\text{m}$  and  $2.43^{+0.09}_{-0.10}$  hr at  $4.5\ \mu\text{m}$  are fully consistent. In contrast, the two rotation periods obtained for 2MASS J0501–00 are quite different— $18.5^{+0.8}_{-0.7}$  hr at  $3.6\ \mu\text{m}$  and  $14.7^{+0.9}_{-0.8}$  hr at  $4.5\ \mu\text{m}$ . While the longer period fits the  $3.6\ \mu\text{m}$  well, it does not provide a good fit to the  $4.5\ \mu\text{m}$  data. The shorter period does a better job of fitting both channels. To estimate the most accurate rotation period for 2MASS J0501–00, we fit a sinusoidal model to both channels simultaneously, finding a period of  $15.7 \pm 0.2$  hr. We show the

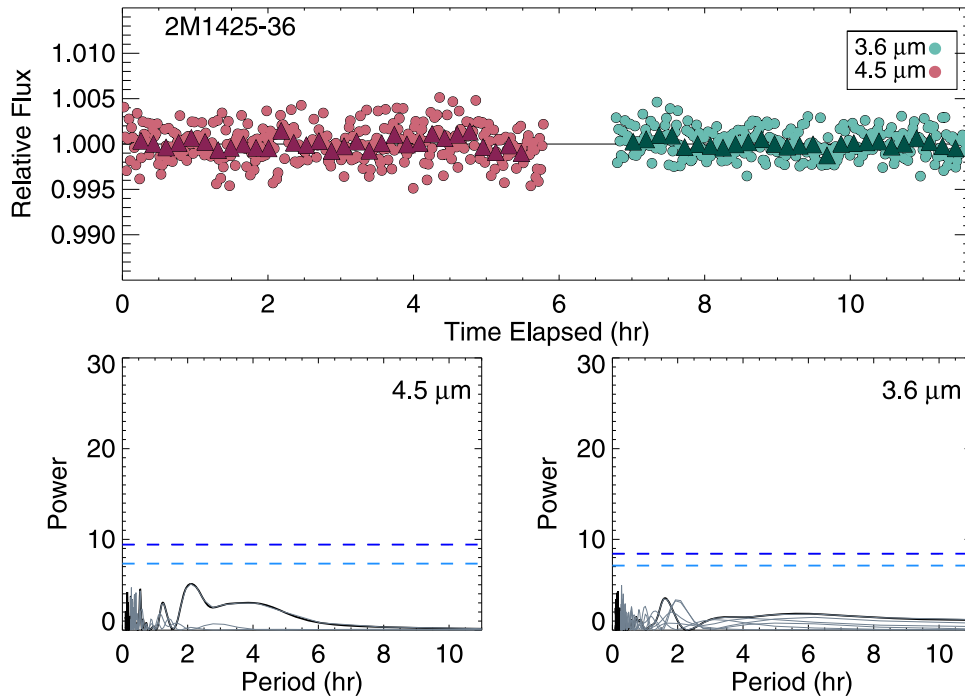


**Figure 5.** Top panel: full corrected Spitzer light curve of 2MASS J1425–36. The  $3.6\ \mu\text{m}$  data are shown in green, and the  $4.5\ \mu\text{m}$  data are shown in pink. Circles show 30 s cadence and triangles show 10 minutes cadence. Bottom panels: periodograms for each observation. The target periodogram is shown in black, reference star periodograms are shown in gray, and the 95% and 99% significance thresholds are shown by the blue dashed lines. The periodogram of 2MASS J1425–36 does not show a significant peak in either observation.

posterior distribution of the fit in Figure A3. We adopt  $15.7 \pm 0.2\ \text{hr}$  as the most likely rotation period.

#### 4.4. Fitting the Intrapixel Phase Effect and Astrophysical Variability Simultaneously

The pixel-phase effect can in principle be covariant with astrophysical variability (Heinze et al. 2013). For the variable objects 2MASS J0045+16 and 2MASS J0501–00, it is possible that in correcting for the pixel-phase effect using Equation (1), the variability signal may have been distorted. For these targets, we also fit their raw flux using a model that includes the pixel-phase effect (Equation (1)) and a sinusoidal model to represent the variability, following previous Spitzer brown dwarf variability and exoplanet transit studies (e.g., Metchev et al. 2015; Delrez et al. 2018).

We find that simultaneously fitting both the pixel-phase effect and astrophysical variability simultaneously does not significantly affect the variability parameters in Table 2. However, the simultaneous fit yields a higher correlation coefficient between the  $x$ - and  $y$ -pixel positions and the measured flux in all cases, suggesting that including the sinusoidal fit during this step worsens the intrapixel phase-effect correction. We use the BIC framework discussed in Section 4.2 to assess whether the extra sinusoidal parameters are warranted by the data and find that the pixel-phase effect model (i.e., Equation (1)) is very strongly favored for each observation. This is likely because the pixel-phase effect has a much larger effect on the photometry than the low-amplitude astrophysical variability. Because the results of the simultaneous fit are more highly correlated with pixel position than the original fit, we use the light curves obtained using the cubic correction model (Equation (1)) for the rest of the analysis.

#### 5. Assessing the Evidence for Phase Shifts between Channels

We investigate the possibility of phase shifts between the  $3.6\ \mu\text{m}$  and  $4.5\ \mu\text{m}$  light curves. Different wavelengths probe different pressure levels in brown dwarf atmospheres (Buenzli et al. 2012), and phase shifts can potentially provide valuable information on the vertical atmospheric structure. Phase shifts have been observed in a number of brown dwarfs over the  $1\text{--}5\ \mu\text{m}$  wavelength range (Buenzli et al. 2012; Yang et al. 2016; Biller et al. 2018), but have not been reported between Spitzer Channels 1 and 2 (Metchev et al. 2015; Yang et al. 2016). Because the  $3.6$  and  $4.5\ \mu\text{m}$  bands probe similar atmospheric pressures (Yang et al. 2016), phase shifts are not generally expected at these wavelengths.

The BIC framework described in Section 4.2 also provides a robust method to determine whether the data warrant the addition of a phase shift between the  $3.6$  and  $4.5\ \mu\text{m}$  light curves for 2MASS J0045+16 and 2MASS J0501–00. The two models allow the variability amplitude to change between the  $3.6$  and  $4.5\ \mu\text{m}$  light curves, but keep the period constant over both observations. The phase-shift model includes an additional phase-shift parameter for the  $3.6\ \mu\text{m}$  data. The BIC is particularly useful in this case as it will penalize the phase-shift model for having an additional parameter. For 2MASS J0501–00, we calculated  $\Delta\text{BIC} = \text{BIC}_{\text{sin}} - \text{BIC}_{\text{phase shift}} = -25$ , i.e., the sinusoidal model without a phase shift is strongly favored. For 2MASS J0045+16, we find  $\Delta\text{BIC} = \text{BIC}_{\text{sin}} - \text{BIC}_{\text{phase shift}} = 5$ . In this case, the model that includes a phase shift between the light curves is positively favored, but this is not a significant result. We conclude that neither 2MASS J0045+16 nor 2MASS J0501–00 shows a significant phase shift between their  $3.6\ \mu\text{m}$  and  $4.5\ \mu\text{m}$  light curves.

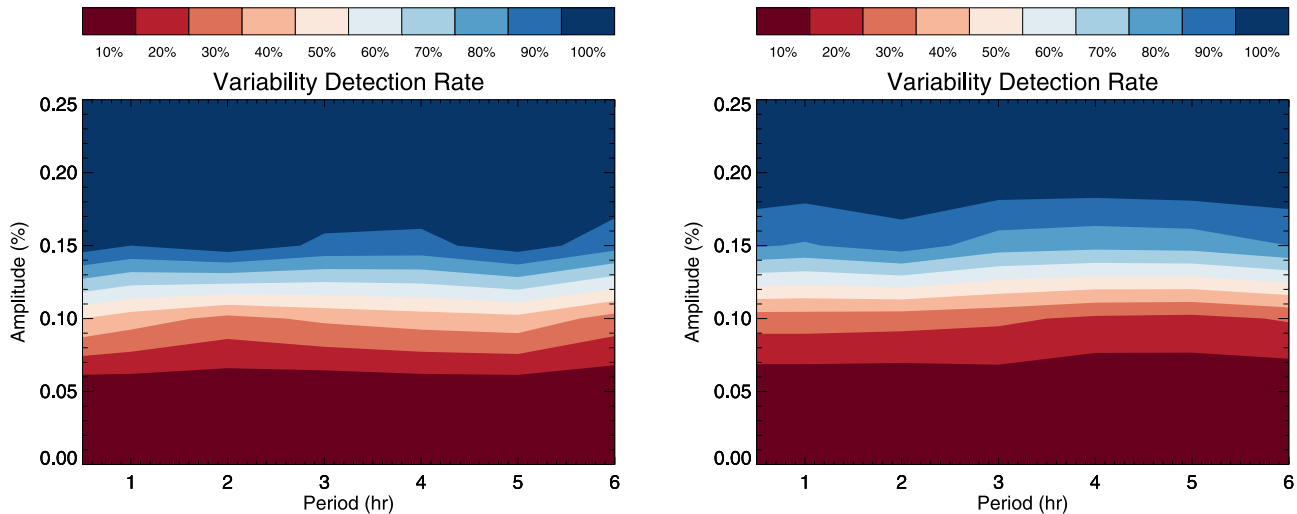


**Figure 6.** Sensitivity plots for the Spitzer  $3.6\ \mu\text{m}$  (left) and  $4.5\ \mu\text{m}$  (right) observations of 2MASS J1425–36. The color scale shows the variability detection probability as a function of amplitude and period. Adopting a detection probability of 90% as our threshold, we place upper limits of 0.16% and 0.18% on the  $3.6\ \mu\text{m}$  and  $4.5\ \mu\text{m}$  variability amplitudes, respectively.

## 6. Comparison with Near-IR Variability Detections

We previously detected variability in all three targets in our ground-based,  $J$ -band survey for variability in low-gravity brown dwarfs (Vos et al. 2019). Ground-based photometric monitoring is an excellent method for detecting variable objects in the near-IR, but due to shorter observation windows and weather constraints, space-based monitoring with Spitzer is more effective at measuring rotation periods, particularly for low-gravity brown dwarfs which are thought to have longer rotation periods (e.g., Vos et al. 2018). In Vos et al. (2019), we detected significant  $J$ -band variability in 2MASS J0045+16 during two  $\sim 4$  hr epochs separated by 2 yr. We measured an amplitude of  $\sim 1\%$  during both observations and found no evidence for light-curve evolution between the two epochs. Our Spitzer light curve appears sinusoidal over the entire observation, so it seems that both the  $J$ -band and mid-IR light curves are stable. Periodogram analysis of the ground-based  $J$ -band light curve suggested a rotation period of 3–6 hr (Vos et al. 2019), while in this paper we measure a period of  $2.4 \pm 0.1$  hr. Both of the ground-based,  $J$ -band light curves have significant gaps in the data due to poor weather during the observation, and this may explain the discrepancy between the estimated ground-based  $J$ -band and measured Spitzer rotation period.

We detected  $J$ -band variability in 2MASS J0501–00 in two epochs in Vos et al. (2019). During each  $\sim 4$  hr observation, we detected a slow downward trend, with a maximum  $J$ -band amplitude of  $\sim 2\%$ . Because we did not cover a full rotation period in either observation, our periodogram analysis constrained the period to  $> 5$  hr, which is consistent with our much longer Spitzer measurement of  $15.07 \pm 0.2$  hr. 2MASS J0501–00 exhibits higher  $J$ -band and Spitzer mid-IR amplitudes than 2MASS J0045+16.

2MASS J1425–36 was the lowest-amplitude variable presented in Vos et al. (2019). We detected variability during one epoch only, with an amplitude of  $\sim 0.7\%$ . Our ground-based  $J$ -band monitoring did not cover a full rotation period, and our periodogram analysis favored periods of 2–4 hr (Vos et al. 2019). We do not detect mid-IR variability in this object and place upper limits on the variability amplitude in each channel. Comparing the near-IR and mid-IR amplitudes of all

three L dwarfs observed in this paper reveals that 2MASS J0501–00 shows the highest mid-IR and near-IR amplitudes, followed by 2MASS J0045+16, and 2MASS J1425–36 shows the lowest amplitudes. All three targets show smaller amplitudes in the mid-IR than the  $J$  band, which is consistent with such amplitude measurements in young and field brown dwarfs (Metchev et al. 2015; Biller et al. 2018). Atmospheric models predict that the  $J$  band probes deeper pressure levels than mid-IR wavelengths, which would explain the lower mid-IR amplitudes (Buenzli et al. 2012).

## 7. Mid-IR Variability Amplitudes of Young L Dwarfs

Observed variability amplitudes are thought to vary with spectral type (Radigan et al. 2014; Metchev et al. 2015), inclination angle (Vos et al. 2017), and surface gravity (Metchev et al. 2015; Vos et al. 2019). In Table 3, we show the full sample of brown dwarfs with measured variability amplitudes and/or upper limits on infrared variability. This table includes their infrared amplitudes, rotation periods, estimated ages, and inclination angles. Figure 7 shows the full sample of field brown dwarfs and young brown dwarfs with measured Spitzer variability amplitudes on a spectral-type color diagram. The area of the symbol size is proportional to the observed variability amplitude. Upper limits on the variability amplitudes of brown dwarfs are shown by lighter colored circles with a cross. With the addition of 2MASS J0045+16 and 2MASS J0501–00 at early L spectral types, we can begin to study the variability properties of the low-gravity population across the entire L sequence. While the sample is still relatively small, some tentative trends emerge.

The left panel of Figure 8 shows the measured  $3.6\ \mu\text{m}$  variability amplitudes as a function of spectral type. It is apparent that the maximum amplitudes for both field and young dwarfs increase with cooler spectral type in the L sequence, as noted by Metchev et al. (2015) for the field dwarf population. Metchev et al. (2015) also find a tentative correlation between low gravity and high-amplitude variability for low-gravity objects with spectral types L3–L5.5. However, the current sample of low-gravity variables show similar  $3.6\ \mu\text{m}$  amplitudes to the field dwarf population. It is worth noting that for



**Table 2**  
Variability Parameters of 2MASS J0045+16, 2MASS J0501–00, and 2MASS J1425–36

Target	SpT	Channel	Amplitude (%)	Period (hr)	Phase (rad)	$\Delta\text{BIC}$
2MASS J0045+16	L2 $\gamma$	1	$0.18 \pm 0.04$	$2.37^{+0.08}_{-0.06}$	$1.2^{+0.9}_{-0.7}$	–44
		2	$0.16 \pm 0.04$	$2.43^{+0.09}_{-0.10}$	$2.7 \pm 0.3$	–28
2MASS J0501–00	L3 $\gamma$	1	$0.36 \pm 0.04$	$18.5^{+0.8}_{-0.7}$	$5.0 \pm 0.4$	–212
		2	$0.24 \pm 0.04$	$14.7^{+0.9}_{-0.8}$	$2.6 \pm 0.3$	–69
		1&2	$0.28 \pm 0.02$	$15.7 \pm 0.2$	$3.1 \pm 0.1$	
2MASS J1425–36	L4 $\gamma$	1	$<0.16$	$<5.6$	...	17
		2	$<0.18$	$<5.6$	...	17

**Note.** Values for 2MASS J0045+16 and 2MASS J0501–00 were obtained using a sinusoidal model MCMC fit. Values for 2MASS J1425–36 were found from the sensitivity plots shown in Figure 6 and from the rotational velocity measurements discussed in Section 2. The  $\Delta\text{BIC}$  values show that the variable, sinusoidal model is strongly favored for 2MASS J0045+16 and 2MASS J0501–00 and the nonvariable, flat model is strongly favored for 2MASS J1425–36.  $\Delta\text{BIC} = \text{BIC}_{\text{sin}} - \text{BIC}_{\text{flat}}$ .

each spectral type, the object with the highest measured amplitude is young—thus, there is the possibility that the highest intrinsic amplitudes occur in young objects, and that the observed amplitudes can be reduced by secondary effects such as inclination angle (Vos et al. 2017).

The right panel of Figure 8 shows the amplitudes of  $4.5\ \mu\text{m}$  variability detections as a function of spectral type. For early-L spectral types, the young population shares similar amplitudes to the field brown dwarfs. In the late-L population, the four young  $\sim\text{L7}$  objects, PSO J318.5–22 (Biller et al. 2018), WISEA 1147–2040, 2MASS 1119–1137AB (Schneider et al. 2018), and VHS1256–12b (Bowler et al. 2020; Zhou et al. 2020), show enhanced amplitudes compared to the field population. Note that because 2MASS 1119–1137AB is a binary system (Best et al. 2017), its peak-to-peak amplitude of 0.96% is likely underestimated as the variability signal may be diluted by its unresolved companion.

In the near-IR, there seems to be a distinction between the behavior of late-L young brown dwarfs and that of field brown dwarfs. While older mid- to late-L dwarfs (Yang et al. 2016; Manjavacas et al. 2018) show a linear amplitude dependence on wavelength, the young objects PSO J318.5–22 (Biller et al. 2018), WISEP J004701.06+680352.1 (W0047, Lew et al. 2016), and HD 203030B (Miles-Páez et al. 2019) show different amplitudes in the water absorption band at  $1.4\ \mu\text{m}$ . PSO J318.5–22 and W0047 both show decreased amplitudes in the water band, while HD 203030B shows a marginal enhancement in amplitude in the water band. Furthermore, the water-band variability amplitude of PSO J318.5–22 appears to change between two rotations, initially showing a suppressed amplitude followed by an amplitude similar to the continuum amplitude in the following rotation (Biller et al. 2018). Miles-Páez et al. (2019) suggest that this may be due to increased height differentiation between the condensate cloud layers and the high-altitude water and carbon monoxide layer in low-gravity objects. This would result in higher variability amplitudes for the young objects in wavelength regions that are relatively free of water and carbon monoxide gas species. Enhanced variability amplitudes have indeed been observed in the  $J$  band (Vos et al. 2019). In the mid-IR, however, we tentatively observe enhanced amplitudes in late-L low-gravity objects at  $4.5\ \mu\text{m}$  but not at  $3.6\ \mu\text{m}$ . More extensive mid-IR monitoring programs will be essential to statistically compare the amplitudes between the two populations at  $3.6$  and  $4.5\ \mu\text{m}$ .

Figure 9 shows variability amplitude ratios ( $A_J$ ,  $A_{3.6}$ ,  $A_{4.5}$ ) measured for low-gravity and field L dwarfs. The brightness

temperature of L dwarf atmospheres is strongly dependent on wavelength, and the variability amplitude ratios in the near- and mid-IR have been used to estimate the temperature gradient among cloud layers or between regions of thin and thick clouds (Radigan et al. 2012; Heinze et al. 2013). Metchev et al. (2015) find no correlation between spectral type and  $A_{3.6}/A_{4.5}$  amplitude ratio. The top panel of Figure 9 shows that the new sample of young objects does not have obvious outliers in this plot. The mean  $A_{3.6}/A_{4.5}$  across the L0–T0 range is  $1.2 \pm 0.5$  for field brown dwarfs and  $1.2 \pm 0.6$  for low-gravity objects, thus we see no difference between the two populations. The bottom two panels of Figure 9 show ratios involving  $J$ -band detections. Apart from PSO J318.5–22 (Biller et al. 2018), the mid-IR and  $J$ -band measurements were not taken simultaneously. Because variability amplitudes are known to evolve rapidly in some cases (e.g., Apai et al. 2017), these results should be interpreted with a degree of caution. The middle panel, which shows the  $A_J/A_{3.6}$  amplitude ratio, suggests, by eye, that this ratio may be higher for the young population. The mean  $A_J/A_{3.6}$  amplitude ratio is  $3.3 \pm 1.8$  for the field dwarfs and  $6.4 \pm 1.0$  for the low-gravity objects. While the mean amplitude ratios in this case are significantly different, more simultaneous amplitude measurements are necessary to robustly investigate this possible trend. Finally, the bottom panel shows the  $A_J/A_{4.5}$  amplitude ratios for variable L dwarfs. The mean amplitude ratio is  $3.7 \pm 1.8$  for the field dwarfs and  $4.9 \pm 3.2$  for the low-gravity sample, so we find no evidence of a difference between the samples. Future simultaneous variability observations with James Webb Space Telescope/NIRcam in the long- and short-wavelength channels may shed light on the amplitude ratios of variability in brown dwarfs in the future.

## 8. Inclination Angles of Variable Brown Dwarfs

Combining our measurements for the rotation period and rotational velocity with a radius estimate allows us to place constraints on the inclination angles of our targets. Filippazzo et al. (2015) provide radius estimates for all three targets. They combine their calculated bolometric luminosity ( $L_{\text{bol}}$ ) with the inferred age of each target to find the range of predicted radii from evolutionary models. Radii estimates, which depend on gas and condensate chemistry, molecular opacities, cloud modeling, and atmospheric boundary conditions (Saumon & Marley 2008), can be heavily dependent on the models. To address this, Filippazzo et al. (2015) use the solar-metallicity, hybrid cloud (SMHC08) models (Saumon & Marley 2008), the

**Table 3**  
Brown Dwarf Variability Detections and Upper Limits in the Infrared

Target	SpT	$A_J$ (%)	$A_{3.6}$ (%)	$A_{4.5}$ (%)	Period (hr)	Age (Myr)	Radius <sup>a</sup> ( $R_{\text{Jup}}$ )	Companion	Inclination ( $^\circ$ )	Variability References
2MASS J00132229−1143006	T2 (T3.5+T4.5?)	$4.6 \pm 0.2$	...	...	>2.8	1000	...	0	...	(1)
LSPM J0036+1821	L3.5	$1.22 \pm 0.04$	$0.47 \pm 0.05$	$0.19 \pm 0.04$	$2.7 \pm 0.3$	1000	$1.01 \pm 0.07$	0	$51 \pm 9$	(2), (3), (4)
2MASS J00452143+1634446	L2	$1.0 \pm 0.1$	$0.18 \pm 0.04$	$0.16 \pm 0.04$	$2.4 \pm 0.1$	50	$1.62 \pm 0.06$	0	$23 \pm 1$	(5), (6)
2MASS J00470038+6803543	L9	8	$1.07 \pm 0.04$	...	$16.4 \pm 0.2$	$130 \pm 20$	$1.28 \pm 0.02^8$	0	$85_{-9}^{+5}$	(7), (4), (8)
2MASS J00501994−3322402	T7	...	<0.59	$1.07 \pm 0.11$	$1.55 \pm 0.02$	1000	$0.94 \pm 0.16$	0	...	(2)
2MASS J0103320+193536	L6	...	$0.56 \pm 0.03$	$0.87 \pm 0.09$	$2.7 \pm 0.1$	$300 \pm 200$	$1.34 \pm 0.13$	0	$40 \pm 8$	(2)
2MASS J01075242+0041563	L8	...	$1.27 \pm 0.13$	$1 \pm 0.2$	$5 \pm 2$	1000	$0.98 \pm 0.11$	0	$56 \pm 17$	(2)
GU PSC B	T3.5	$4 \pm 1$	...	...	...	$130 \pm 20$	...	1	...	(9)
SIMP J013656.57+093347.3	T2.5	4.5	$1.5 \pm 0.2$	...	$2.414 \pm 0.078$	$200 \pm 50$	$1.22 \pm 0.01^{12}$	0	$80 \pm 12$	(10), (11), (12), (13), (4)
2MASS J01383648−0322181	T3	$5.5 \pm 1.2$	...	...	...	1000	...	0	...	(2)
SDSS J015141.69+124429.6	T0.0	...	<0.83	<0.81	...	1000	$0.97 \pm 0.16$	0	...	(2)
2MASSW J0310599+164816	L8	...	...	...	...	1000	...	0	...	(14)
SDSS J042348.57−041403.5	L6.5+T2	$0.8 \pm 0.08$	...	...	$2 \pm 0.4$	1000	...	0	$79_{-16}^{+11}$	(15), (4)
PSO J071.8769−12.2713	T2	$4.5 \pm 0.6$	...	...	...	...	...	0	...	(6)
2MASS J05012406−0010452	L4	$2 \pm 1$	$0.36 \pm 0.04$	$0.24 \pm 0.04$	$15.7 \pm 0.2$	$300 \pm 200$	$1.38 \pm 0.18$	0	$73_{-12}^{+17}$	(5), (6)
2MASS J05591914−1404488	T4.5	$0.7 \pm 0.5$	...	...	$10 \pm 3$	1000	$0.97 \pm 0.11$	0	...	(10)
2MASS J06244595−4521548	L6.5	>1	...	...	...	1000	$0.99 \pm 0.10$	0	...	(14)
SDSS J075840.33+324723.4	T0.0+T3.5	$4.8 \pm 0.2$	...	...	$4.9 \pm 0.2$	1000	...	0	...	(10)
DENIS J081730.0−615520	T6	$0.6 \pm 0.1$	...	...	$2.8 \pm 0.2$	1000	$0.94 \pm 0.16$	0	...	(10)
2MASSW J0820299+450031	L5	...	<0.4	<0.48	...	1000	...	0	...	(2)
2MASS J0825196+211552	L7.5	>1	$0.81 \pm 0.08$	$1.4 \pm 0.3$	$7.6 \pm 5$	1000	$0.98 \pm 0.11$	0	...	(2)
SDSS J085834.42+325627.7	T1	...	<0.27	<0.64	...	1000	...	0	...	(2)
2MASS J09490860−1545485	T1.0+T2.0	...	<0.54	<0.83	...	1000	$0.96 \pm 0.17$	0	...	(2)
LP261−75B	L6V	$2.4 \pm 0.14$	...	...	$4.78 \pm 0.98$	$30 \pm 50$	...	1	...	(16)
2MASS J10101480−0406499	L6	$3.6 \pm 0.4$	...	...	...	1000	$0.94 \pm 0.16$	0	...	(11)
SDSS J104335.08+121314.1	L9	...	$1.54 \pm 0.15$	$1.2 \pm 0.2$	$3.8 \pm 0.2$	1000	$0.98 \pm 0.11$	0	...	(2)
WISE 1049B	L7.5	...	...	...	$4.87 \pm 0.01$	1000	$1.02 \pm 0.07$	0	$83_{-8}^{+7}$	(17), (18), (4)
SDSS J105213.51+442255.7	L6.5+T1.5	$2.2 \pm 0.5$	...	...	$3 \pm 0.5$	1000	...	0	...	(19)
DENIS-P J1058.7−1548	L2.5	$0.8 \pm 0.1$	$0.39 \pm 0.04$	<0.3	$4.1 \pm 0.2$	1000	$1.00 \pm 0.07$	0	$90_{-2}^{+0}$	(20), (2), (4)
2MASS J10595185+3042059	T8	...	<0.83	<0.89	...	1000	...	0	...	(2)
SDSS J111009.99+011613.0	T5.5	...	...	<1.25	...	$130 \pm 20$	$1.24 \pm 0.04$	0	...	(8)
2MASS J11193254−1137466AB	L7	...	$0.46 \pm 0.036$	$0.96 \pm 0.037$	$3.02 \pm 0.04$	$7 \pm 2.5$	...	0	...	(21)
2MASS J11220826−3512363	T2	...	<0.24	<0.31	...	1000	...	0	...	(2)
2MASS J11263991−5003550	L5	$1.2 \pm 0.1$	$0.21 \pm 0.04$	$0.29 \pm 0.15$	$3.2 \pm 0.3$	1000	...	0	$35 \pm 7$	(10), (2), (4)
WISEA J114724.10−204021.3	L7	...	$1.596 \pm 0.08$	$2.216 \pm 0.09$	$19.39 \pm 0.3$	$7 \pm 2.5$	...	0	...	(21)
SDSS J115013.17+052012.3	L6	...	<0.38	<0.65	...	1000	...	0	...	(2)
2M1207b	L6	$2.72 \pm 0.1$	...	...	$10.7 \pm 1$	$7 \pm 2.5$	$1.36 \pm 0.02$	1	...	(22)
2MASS J12095613−1004008	T2+T7.5	...	<0.4	<0.56	...	1000	...	0	...	(2)
2MASS J12195156+3128497	L9	>2	...	...	...	1000	...	0	...	(14)
SDSS J125453.90−012247.5	T2	...	<0.15	<0.3	...	1000	$0.98 \pm 0.15$	0	...	(2)
VHS1256−1257b	L7	24.7	...	$5.76 \pm 0.04$	$22.04 \pm 0.05$	150−300	...	1	$90_{-29}^{+0}$	(23), (24)
Ross 458C	T8.5	$2.62 \pm 0.02$	<1.37	<0.72	$6.75 \pm 1.58$	125 $\pm$ 75	...	1	...	(25), (2)
2MASS J13243559+6358284	T2	...	$3.05 \pm 0.15$	$3 \pm 0.3$	$13 \pm 1$	$130 \pm 20$	...	0	...	(2)
WISE J140518.39+553421.3	Y0	...	$7.2 \pm 0.8$	$7.1 \pm 0.2$	$8.2 \pm 0.3$	1000	...	0	...	(26)
ULAS J141623.94+134836.3	T7.5	...	<0.91	<0.59	...	1000	$0.96 \pm 0.16$	0	...	(2)
SDSS J141624.08+134826.7	L6	...	<0.15	<0.22	...	1000	...	0	...	(2)

G

**Table 3**  
(Continued)

Target	SpT	$A_J$ (%)	$A_{3.6}$ (%)	$A_{4.5}$ (%)	Period (hr)	Age (Myr)	Radius <sup>a</sup> ( $R_{\text{Jup}}$ )	Companion	Inclination ( $^\circ$ )	Variability References
2MASS J14252798−3650229	L4	$0.7 \pm 0.3$	$<0.16$	$<0.18$	...	$130 \pm 20$	$1.32 \pm 0.09$	0	$52^{+19}_{-13}$	(5), (6)
2MASSW J1507476−162738	L5	0.7	$0.53 \pm 0.11$	$0.45 \pm 0.09$	$2.5 \pm 0.1$	1000	$0.99 \pm 0.09$	0	$23 \pm 2$	(11), (2), (4)
SDSS J151114.66+060742.9	L5.5+T5.0	...	$0.67 \pm 0.07$	$<0.49$	$11 \pm 2$	1000	...	0	...	(2)
SDSS J151643.01+305344.4	L8.0+L9.5	...	$2.4 \pm 0.2$	$3.1 \pm 1.6$	$6.7 \pm 5$	1000	...	0	...	(2)
SDSS J152039.82+354619.8	T0	...	$<0.3$	$<0.45$	...	1000	...	0	...	(2)
SDSS J154508.93+355527.3	L7.5	...	$<0.59$	$<1.15$	...	1000	...	0	...	(2)
2MASS J16154255+4953211	L4	...	$0.9 \pm 0.2$	$<0.39$	$24 \pm 5$	$300 \pm 200$	$0.94 \pm 0.16$	0	$86^{+4}_{-10}$	(2), (4)
2MASS J16291840+0335371	T2	$4.3 \pm 2.4$	...	...	$6.9 \pm 2.4$	1000	...	0	$82^{+8}_{-12}$	(10), (4)
2MASSW J1632291+190441	L8	...	$0.42 \pm 0.08$	$0.5 \pm 0.3$	$3.9 \pm 0.2$	1000	$0.97 \pm 0.12$	0	...	(2)
2MASSI J1721039+334415	L5.3	...	$0.33 \pm 0.07$	$<0.29$	$2.6 \pm 0.1$	1000	...	0	$27 \pm 4$	(2), (4)
2MASSI J1726000+153819	L2	...	$<0.29$	$<0.49$	...	$300 \pm 200$	$1.40 \pm 0.20$	0	...	(2)
WISEP J173835.52+273258.9	Y0	...	...	$3 \pm 0.1$	$6 \pm 0.1$	1000	...	0	...	(27)
2MASS J17502484−0016151	L5	$>1$	...	...	...	1000	...	0	...	(14)
2MASS J17503293+1759042	T3.5	$>1$	...	...	...	1000	$0.97 \pm 0.16$	0	...	(14)
2MASS J17534518−6559559	L4	...	$<0.25$	...	...	1000	...	0	...	(2)
2MASS J18212815+1414010	L5	...	$0.54 \pm 0.05$	$0.71 \pm 0.14$	$4.2 \pm 0.1$	1000	...	0	$61 \pm 17$	(11), (2), (4)
2MASS J18283572−4849046	T5.5	$0.9 \pm 0.1$	...	...	$5 \pm 0.6$	1000	$0.95 \pm 0.16$	0	...	(10)
2MASS J20025073−0521524	L5.5	$1.7 \pm 0.2$	...	...	...	$300 \pm 200$	...	0	...	(5)
SDSS J204317.69−155103.4	L9.5	...	$<0.71$	$<0.74$	...	1000	...	0	...	(2)
SDSS J205235.31−160929.8	T1+T2.5	...	$<0.36$	$<0.71$	...	1000	...	0	...	(2)
PSO 318.5−22	L7	$10 \pm 1.3$	...	$3.4 \pm 0.08$	$8.61 \pm 0.06$	$23 \pm 3$	$1.41 \pm 0.03$	0	$56 \pm 8$	(28), (29), (5)
2MASS J21392676+0220226	L8.5+T3.5	$26 \pm 1$	$11 \pm 1$	$10 \pm 1$	$7.618 \pm 0.18$	1000	$0.96 \pm 0.16$	0	$90^{+0}_{-1}$	(10), (13), (4), (11)
HN PegB	T2.5	1.2	$0.77 \pm 0.15$	$1.1 \pm 0.5$	$15.4 \pm 0.5$	$237 \pm 33$	...	1	...	(2)
2MASS J21481628+4003593	L7	...	$1.33 \pm 0.07$	$1.03 \pm 0.1$	$19 \pm 4$	$200 \pm 200$	$0.99 \pm 0.10$	0	$88^{+2}_{-8}$	(2), (4)
2MASSW J2208136+292121	L2	...	$0.69 \pm 0.07$	$0.54 \pm 0.11$	$3.5 \pm 0.2$	$23 \pm 3$	$1.41 \pm 0.20$	0	$55 \pm 10$	(2), (4)
2MASS J22153705+2110554	T1 (T0+T2?)	$10.7 \pm 0.4$	...	...	...	1000	...	0	...	(2)
2MASSW J2224438−015852	L4.5V	...	$<0.1$	$<0.15$	...	1000	$0.99 \pm 0.08$	0	...	(2)
2MASS J22282889−4310262	T6.5	5.3	$4.6 \pm 0.2$	$1.51 \pm 0.15$	$1.41 \pm 0.01$	1000	$0.94 \pm 0.16$	0	...	(10), (2), (30)
2MASS J22393718+1617127	T3	$5.8 \pm 0.4$	...	...	...	1000	...	0	...	(2)
2MASS J2244316+204343	L6−L8	$5.5 \pm 0.6$	$0.8 \pm$	...	$11 \pm 2$	120	$1.28 \pm 0.02^8$	0	$76^{+14}_{-20}$	(31), (8), (5)
SDSSp J224953.45+004404.2	L3+L5	...	$<0.25$	$<0.45$	...	1000	...	0	...	(2)
2MASSI J2254188+312349	T5.0	...	$<0.47$	$<0.39$	...	1000	...	0	...	(2)
WISE J085510.83−071442.5	Y2	...	$4 \pm 1$	$4 \pm 1$	...	1000	...	0	...	(32)
HD 203030B	L7.5	$1.1 \pm 0.3$	...	...	$7.5 \pm 0.6$	$9 \pm 60$	...	1	...	(33)

**Notes.**

<sup>a</sup> Estimated radii are from Filipazzo et al. (2015), except where a superscript indicates reference.

**References.** (1) Eriksson et al. (2019); (2) Metchev et al. (2015); (3) Croll et al. (2016); (4) Vos et al. (2017); (5) Vos et al. (2019); (6) This work; (7) Lew et al. (2016); (8) Vos et al. (2018); (9) Naud et al. (2017); (10) Radigan et al. (2014); (11) Yang et al. (2016); (12) Gagné et al. (2017); (13) Apai et al. (2017); (14) Buenzli et al. (2014); (15) Clarke et al. (2008); (16) Manjavacas et al. (2018); (17) Gillon et al. (2013); (18) Buenzli et al. (2015); (19) Girardin et al. (2013); (20) Heinze et al. (2013); (21) Schneider et al. (2018); (22) Zhou et al. (2016); (23) Bowler et al. (2020); (24) Zhou et al. (2020); (25) Manjavacas et al. (2019); (26) Cushing et al. (2016); (27) Leggett et al. (2016); (28) Allers et al. (2016); (29) Biller et al. (2018); (30) Buenzli et al. (2012); (31) Morales-Calderón et al. (2006); (32) Esplin et al. (2016); (33) Miles-Páez et al. (2019).

(This table is available in its entirety in machine-readable form.)

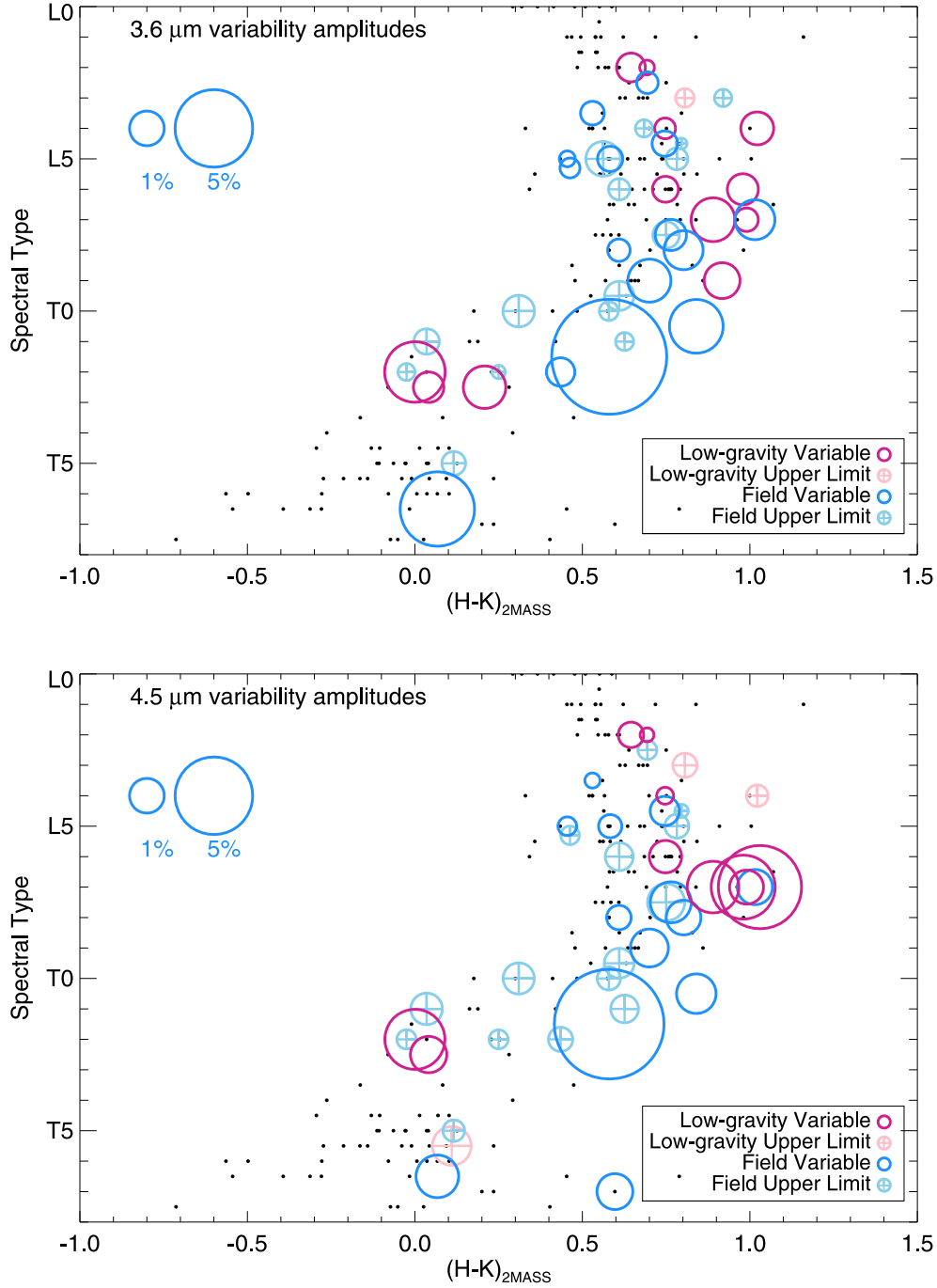


**Figure 7.** Brown dwarfs with Spitzer detections of variability as a function of spectral type and  $(H - K)_{2\text{MASS}}$  color. Black points show the field L–T dwarf sequence from Dupuy & Liu (2012). The sample of field brown dwarfs with detected mid-IR variability is shown by the dark blue circles, and the sample of young mid-IR variables is shown in dark pink. Variability amplitude upper limits are shown for the field and young populations in light blue and light pink circles with crosses, respectively. The symbol area is proportional to the variability amplitude. The data used for this figure are shown in Table 3.

DUSTY00 models (Chabrier et al. 2000), and the  $f_{\text{sed}} = 2$  (SMf208) models (Saumon & Marley 2008) to estimate the radii. Their final radius range for each source is the minimum and maximum values of all three model predictions for the given age and  $L_{\text{bol}}$ , and are not formal  $1\sigma$  uncertainties. The range of estimated radii for the field brown dwarfs is in good agreement with the handful of directly measured field dwarf radii (e.g., Pont et al. 2005; Deleuil et al. 2008; Bouchy et al. 2010; Siverd et al. 2012; Littlefair et al. 2014); however, there has not yet been an empirical test of the radii of young (<400 Myr) objects. Thus, for the young objects in particular,

it is possible that the radii, and therefore the inclinations, may be biased in some way.

We use Monte Carlo analysis to calculate the inclination of each target using normal distributions for the periods and radii, and the  $\nu \sin(i)$  distributions obtained in Section 2.  $\sin(i)$  values that fell above 1 were set equal to 1 because discarding them biased the results to lower inclination angles. The inclination and error were calculated from the median and standard deviation of the resulting distribution of  $\sin(i)$ . Because we did not detect significant variability for 2MASS J1425–36, we do not have a measured rotation period. However, we can set a



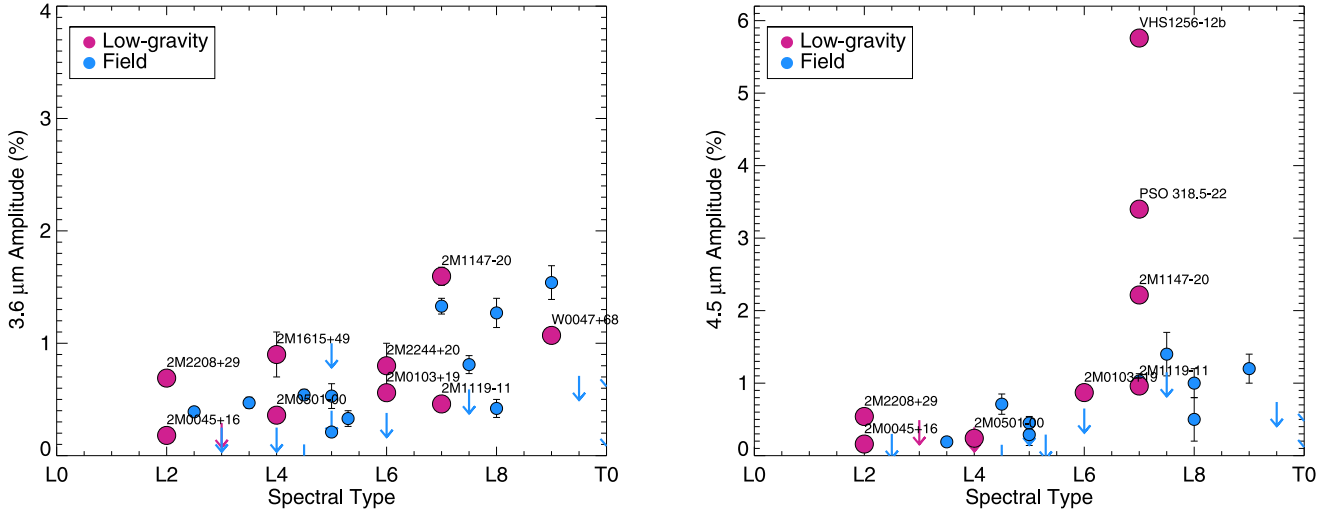


**Figure 8.** Spitzer peak-to-peak variability amplitudes as a function of spectral type for L dwarfs. Variability amplitude upper limits are shown for the field and young populations by downward-pointing arrows. Low-gravity 3.6  $\mu\text{m}$  detections (left) follow the same trend as the field brown dwarfs—increasing amplitude with cooler spectral type. However, the 4.5  $\mu\text{m}$  detections show a tentative enhancement in amplitude at late-L spectral types for low-gravity objects only.

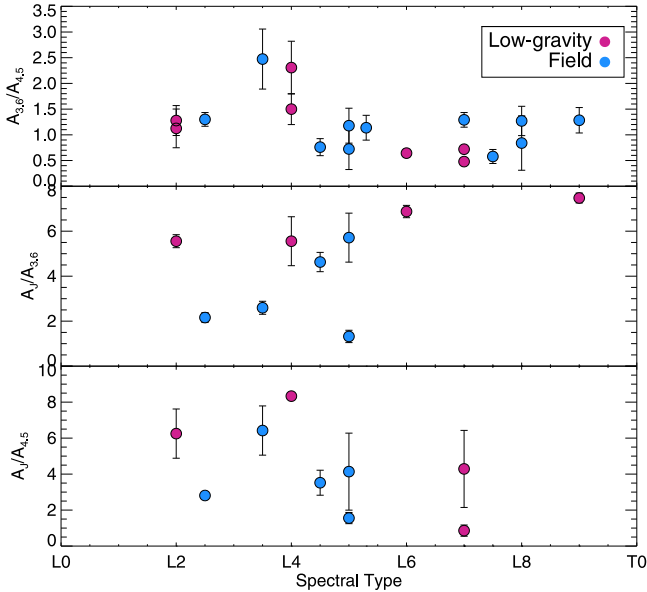


**Figure 9.** Variability amplitude ratios of field and young brown dwarfs. We do not find any significant correlations between variability amplitudes in the  $J$  band, at 3.6 and 4.5  $\mu\text{m}$  for young and field dwarfs.

lower limit on the rotation period of 2.5 hr based on our ground-based variability detection (Vos et al. 2019) and an upper limit from our  $v \sin(i)$  measurement (Section 2). We compute the inclination angle of 2MASS J1425–36 using the method described above, but we used a uniform distribution of 2.5–5.6 hr for the rotation period based on our  $J$ -band light curve published in Vos et al. (2019) and the maximum period determined from our  $v \sin(i)$  measurement.

We show our input values for  $v \sin(i)$ , period, and radius, and our resulting inclination angles in Table 1. We find that 2MASS J0045+16 has an inclination angle of  $22^\circ \pm 1^\circ$ , placing it close to a pole-on alignment. We calculate an inclination angle of  $60^{+20}_{-9}^\circ$  for 2MASS J0501–00. This inclination is less accurate due to the large error bar on the rotation period, but 2MASS J0501–00 is clearly closer to equator on than 2MASS J0045+16. We find that 2MASS

J1425–36 is inclined with an angle of  $54^{+36}_{-15}^\circ$ ; however, a rotation period measurement is necessary to confirm this inclination angle.

### 8.1. Are the Inclination Angles Randomly Aligned?

Our total sample of 18 objects with measured inclinations allows us to test whether the sample is inconsistent with the expected inclination angles of a sample of randomly oriented sample of objects. This may be expected as equator-on objects tend to show higher variability amplitudes (Vos et al. 2017) so their rotation periods are more easily detected and measured with variability observations. Moreover, brown dwarfs that are inclined pole on should not exhibit variability due to rotational modulation of atmospheric inhomogeneities, and this is evident by our lack of detections in brown dwarfs with inclinations  $< 20^\circ$  (Vos et al. 2017). Thus, we would expect that the sample of variable objects should be biased toward equator-on objects. For a sample of objects with random orientations, the probability distribution of inclination angles is  $P(i) \sim \sin(i)$  (Vos et al. 2017). We perform a 1D Kolmogorov–Smirnov test to determine if the measured inclination angles differ significantly from a randomly oriented distribution of inclination angles (shown in Figure 10). We find a Kolmogorov–Smirnov test statistic of  $\sim 0.18$  and a significance level of 0.5. Thus, there is currently no evidence that the sample of measured inclinations differs from that expected from randomly oriented objects. This will be a useful test to run as a larger sample of inclination angles are measured in the future.

### 8.2. The Variability Amplitude is Influenced by the Inclination Angle

The addition of three more objects with measured variability in the mid-IR and measured inclination allows us to further test the relationships between inclination, variability amplitude, and color anomaly introduced by Vos et al. (2017). In the left panel of Figure 11, we update the plot showing the tentative relation between inclination angle and [3.6] variability amplitude, and in the right panel of Figure 11, we present the equivalent plot for [4.5] variability data. Both plots show that the population of high-amplitude variables are viewed close to equator on ( $90^\circ$ ),

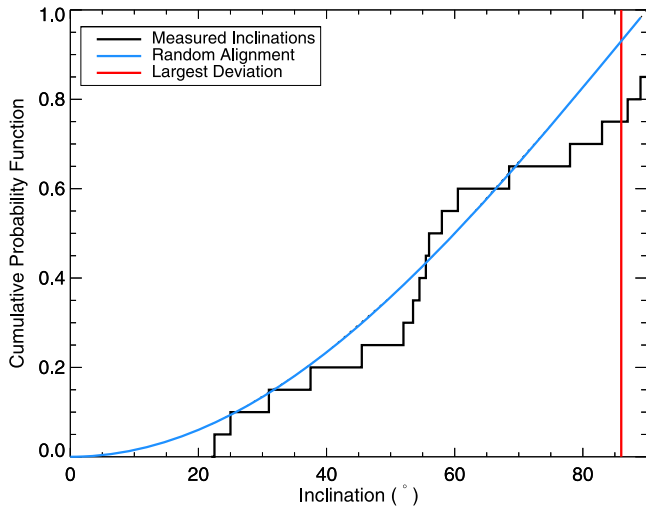


**Figure 10.** The cumulative probability distribution for a sample of objects with random orientation (blue) compared to the measured sample of brown dwarf inclination angles (black). The Kolmogorov–Smirnov test results in a maximum deviation of  $\sim 0.18$  at  $86^\circ$  and a significance of 0.5. Our results show that there is no significant difference between the two distributions.

while the maximum variability amplitudes decrease as the object is viewed closer to pole on ( $0^\circ$ ).

We test the significance of the inclination dependence of the variability amplitude using the two-dimensional two-sample Kolmogorov–Smirnov test (Peacock 1983; Fasano & Franceschini 1987), which is used to assess the null hypothesis that two samples are drawn from the same two-dimensional distribution. We simulate a random distribution of inclinations and amplitudes with the same sample size and ranges as our data in Figure 11. The two-dimensional Kolmogorov–Smirnov test outputs a test statistic, which is a measure of the cumulative probability difference between the two distributions, and the  $p$ -value, the probability that the two samples are drawn from the same distribution—in our case, this is the probability that the data in Figure 11 are drawn from a random sample. We run the two-dimensional Kolmogorov–Smirnov test on the  $3.6$  and  $4.5 \mu\text{m}$  data 1000 times each to obtain a distribution of the test statistic and  $p$ -value in each case. For the  $3.6 \mu\text{m}$  data, we find a Kolmogorov–Smirnov test statistic of 0.8 with a  $p$ -value of  $2 \times 10^{-5}$ , indicating that the data are significantly different from a random sample of inclinations and amplitudes. Similarly, the  $4.5 \mu\text{m}$  data give a test statistic of 0.8 with a  $p$ -value of  $4 \times 10^{-5}$ . Thus, the effect of inclination angle on the measured variability amplitude appears to be highly significant. The large body of variability studies carried out to date has shown that the variability properties of brown dwarfs are affected by fundamental properties such as temperature (e.g., Radigan et al. 2014; Metchev et al. 2015) and gravity (e.g., Biller et al. 2018; Vos et al. 2019). In Figure 11, this is evident by the range of amplitudes that have been observed in objects that are viewed with inclination angles close to  $90^\circ$ . Our analysis shows that inclination is a secondary effect that reduces the intrinsic variability signal for objects not viewed equator on.

### 8.3. The Relation between Inclination Angle and Color Anomaly

We additionally examine the relation between inclination and color anomaly in Figure 12. The color anomaly of a brown

dwarf is defined as the median  $(J - K)_{2\text{MASS}}$  color of brown dwarfs with the same spectral type and gravity class subtracted from the  $(J - K)_{2\text{MASS}}$  color of the object (Vos et al. 2017). Objects with a positive color anomaly appear redder than the median, and objects with a negative color anomaly appear bluer than the median. Red colors in brown dwarfs are generally explained by the presence of thick clouds or hazes (Gizis et al. 2012; Marley et al. 2012; Hiranaka et al. 2016). Both the young and field dwarfs seem to follow the apparent trend between high inclination and red colors in Figure 12. Following Press et al. (1986), we calculate the Spearman’s  $\rho$  coefficient to determine the significance of this apparent relation. For the field population, we find a correlation coefficient of 0.71 with a  $2.1\sigma$  significance. For the young population, we find a correlation coefficient of 0.73 with a  $2.1\sigma$  significance. For the combined population of both field and young objects, we find a correlation coefficient of 0.76 with a  $3.2\sigma$  significance. As discussed in Vos et al. (2017), one explanation for this correlation would be the accumulation of thicker clouds at the equator relative to the clouds, similar to the zonally banded cloud patterns observed on Jupiter. Recently, Showman et al. (2019) presented global, three-dimensional atmospheric simulations of brown dwarfs and giant planets, showing that atmospheric waves and turbulence interact with the rotation to produce numerous zonal jets. While these models do not include clouds, it is possible that the clouds may couple with these jets to form a zonally banded cloud pattern, as we see on Jupiter (Showman et al. 2019).

## 9. Rotation Periods of Young Brown Dwarfs

We combine our two new rotation periods with the rich sample of variable brown dwarfs to investigate the relations between rotation period and age. Moore et al. (2019) provide a well-vetted sample of brown dwarfs with measured rotation periods with ages ( $<10$  Myr). This young sample includes variable brown dwarfs in the 1 Myr Orion Nebula Cluster reported by Rodríguez-Ledesma et al. (2009), members of the 3–6 Myr Orion Belt region reported by Scholz & Eisloffel (2004, 2005) and Cody & Hillenbrand (2010), members of Upper Sco ( $\sim 10$  Myr, Scholz et al. 2015; Moore et al. 2019), and members of Taurus ( $\sim 1$  Myr, Scholz et al. 2018). Moore et al. (2019) define absolute  $J$ -band magnitude cutoffs to separate brown dwarfs from low-mass stars in this sample. In this  $<10$  Myr sample, the lower-mass limits are at  $\sim 0.02 M_\odot$  (Moore et al. 2019). We point the reader to this paper for a detailed discussion of the vetting procedure for the  $<10$  Myr sample. The intermediate-age (10–500 Myr) sample is compiled from variability monitoring programs reported by Metchev et al. (2015), Zhou et al. (2016, 2018), Biller et al. (2018), Schneider et al. (2018), Vos et al. (2018), and Manjavacas et al. (2019). The field age sample is composed of variable dwarfs reported by Metchev et al. (2015), Yang et al. (2016), Esplin et al. (2016), Cushing et al. (2016), and Leggett et al. (2016). Figure 13 shows the full sample of brown dwarfs with measured rotation periods from 1 Myr to 1 Gyr. For the Orion Nebula Cluster, the Orion Belt region, Upper Sco, and Taurus, we have added a random spread in the ages of each object for clarity. As pointed out by Moore et al. (2019), age uncertainties and age spreads for young clusters, the young moving group, and the field sample are likely sources of error. As previously found by Scholz et al. (2015), Schneider et al. (2018), and Moore et al. (2019), we find that the sample of

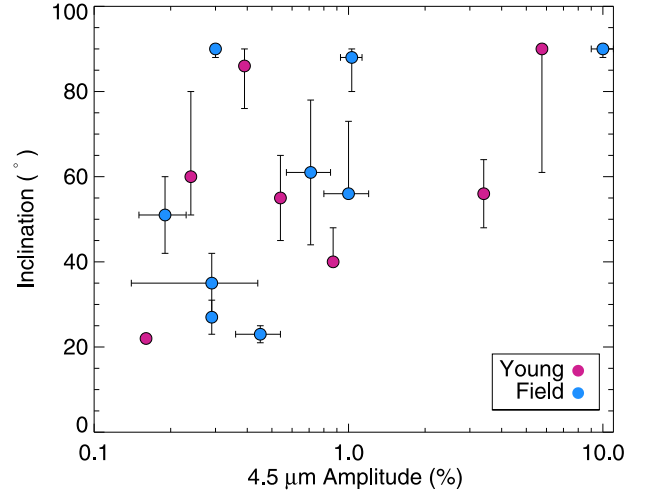
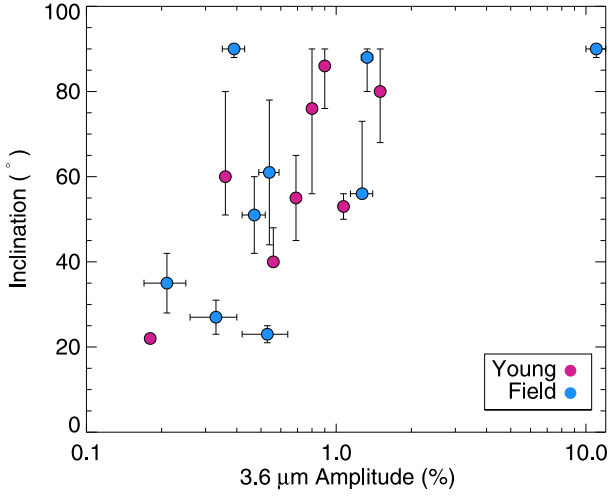


**Figure 11.** Inclination angle plotted against Spitzer [3.6] (left) and [4.5] (right) variability amplitude. The population of high-amplitude variables are viewed close to equator on ( $90^\circ$ ), while the maximum variability amplitudes decrease as the object is viewed closer to pole on ( $0^\circ$ ).

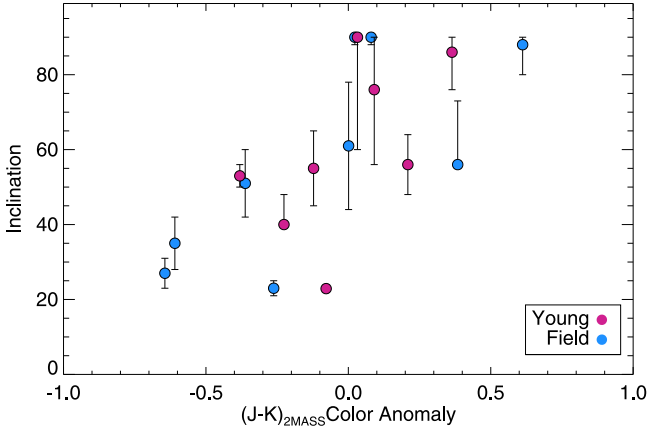


**Figure 12.** Inclination angle plotted against  $(J - K)_{2MASS}$  color anomaly for variable young and field brown dwarfs. The color anomaly of a brown dwarf is defined as the median  $(J - K)_{2MASS}$  color of brown dwarfs with the same spectral type and gravity class subtracted from the  $(J - K)_{2MASS}$  color of the object. We find a tentative correlation between the inclination angle and color, where objects viewed equator on appear redder than the median.

variable brown dwarfs spin up over time, due in part to angular momentum conservation as the objects contract and possible disk locking at very young age ( $<5$  Myr; Scholz et al. 2018).

We investigate whether the current sample of measured rotation periods is consistent with gravitational contraction using evolutionary models and assuming angular momentum conservation (Bouvier et al. 2014; Scholz et al. 2015; Schneider et al. 2018). We use the evolutionary models of Baraffe et al. (2015) to estimate the radii of brown dwarfs at 1 Myr with masses of  $84 M_{Jup}$  and  $10 M_{Jup}$  and the maximum and minimum measured periods from this age group. Assuming angular momentum conservation, we then calculated the expected periods from 1 Myr to 1 Gyr using the predicted radii from Baraffe et al. (2015). Because the Baraffe et al. (2015) models do not reach 1 Gyr for the low-mass objects, we artificially add a final radius data point of  $1 R_{Jup}$  at 1 Gyr. This additional radius value is also added by Schneider et al. (2018) but is not explained in the text. In Figure 13, we plot the period evolution assuming angular momentum conservation for the two brown dwarfs in black.

The lower limit for the rotation period of a rotating object is known as the “breakup period.” We calculate the breakup period by equating the equatorial velocity with the escape velocity (Leggett et al. 2016), which changes in time as the radius contracts. This method assumes a spherical object; however, in reality a rapidly rotating object will experience strong flattening. In Figure 13, we plot the breakup period of a  $10 M_{Jup}$  and  $84 M_{Jup}$  object in red. The brown dwarfs in Figure 13 show a wide spread in rotation period measurements at each age, but the “spin-up” of brown dwarfs with age is evident. Comparing with the angular momentum conservation and breakup limits based on evolutionary models, we see that the general population of brown dwarfs with measured rotation periods agrees with these limits. Additional variability data for members of young moving groups as part of our 30 object Spitzer Program 14128 (PI: J. Faherty, J. M. Vos et al. 2020, in preparation) will allow us to fill in the intermediate-age sample and further investigate the angular momentum evolution of brown dwarfs over their lifetime, and in particular investigate the effects of mass on the spin-up process, as has been studied for the  $<10$  Myr population by Scholz et al. (2018).

## 10. Conclusions

In this paper, we present Spitzer 3.6 and 4.5  $\mu m$  variability monitoring observations of three young L dwarfs previously found to exhibit variability in the near-IR (Vos et al. 2019), 2MASS J0045+16, 2MASS J0501–00, and 2MASS J1425–36.

1. We use new and published high-resolution spectra to measure the rotational velocities of 2MASS J0045+16, 2MASS J0501–00, and 2MASS J1425–36. We combine these  $v \sin(i)$  values with estimated radii to place upper limits on the rotation periods of each target, which guided our Spitzer observation lengths.
2. We detect significant periodic variability in 2MASS J0045+16 and 2MASS J0501–00 at 3.6  $\mu m$  and 4.5  $\mu m$ , but do not detect variability in 2MASS J1425–36.
3. We measure rotation periods of  $2.4 \pm 0.1$  hr for 2MASS J0045+16 and  $15.7 \pm 0.2$  hr for 2MASS J0501–00. Because 2MASS J1425–36 does not show variability in our Spitzer observations, we do not measure a rotation

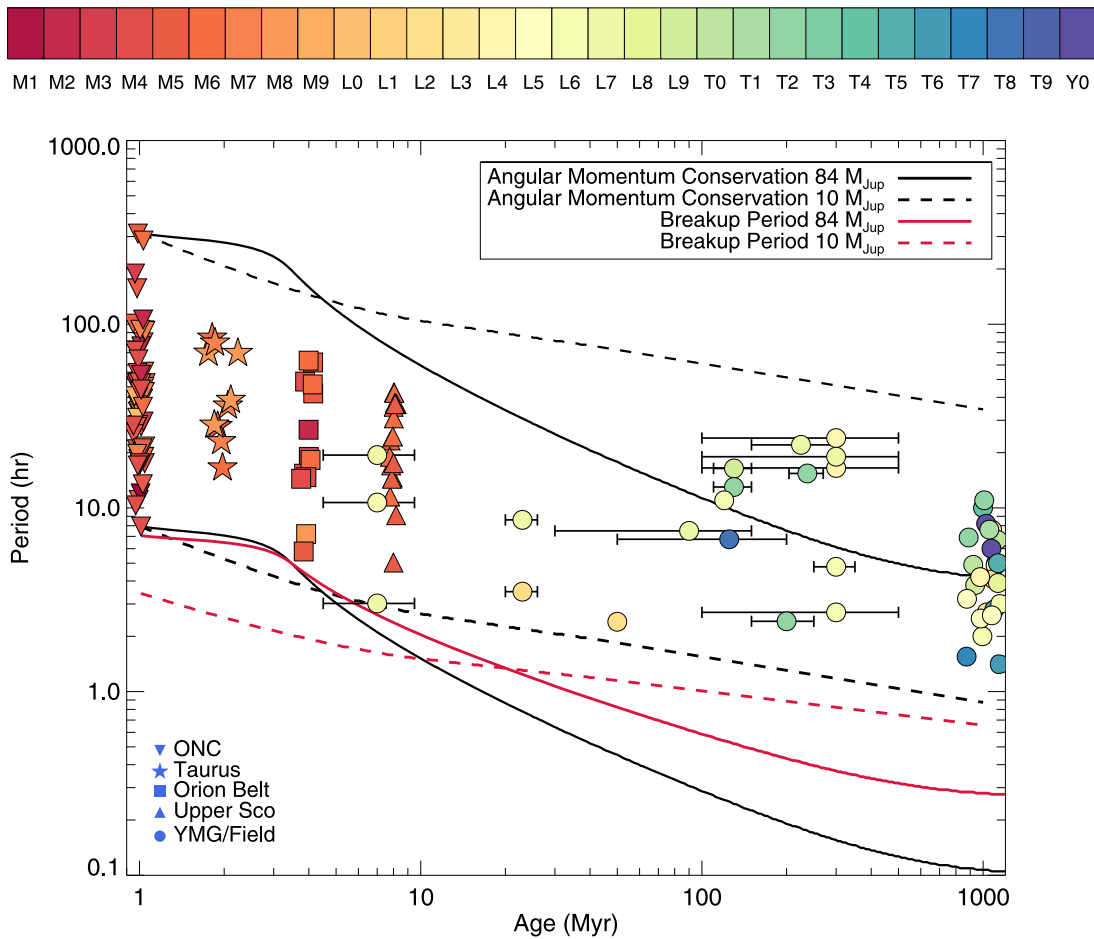


**Figure 13.** Rotation rates of brown dwarfs as a function of age. The ages of the field dwarf sample are not known, and we plot them at 1 Gyr. The ages of younger objects are taken from their parent moving group or cluster. Black lines show the expected rotation period evolution of a  $10 M_{\text{Jup}}$  (dashed) and  $84 M_{\text{Jup}}$  (solid) object assuming conservation of angular momentum, with initial rotation periods as the maximum and minimum periods measured for the 1 Myr sample, and using evolutionary models (Baraffe et al. 2015). The breakup period for masses of  $10 M_{\text{Jup}}$  (dashed) and  $84 M_{\text{Jup}}$  (solid) is plotted in red. The population of brown dwarfs with measured rotation periods agrees with the calculated periods using evolutionary models and assuming angular momentum conservation.

period for this object. However, based on our earlier ground-based monitoring and measured  $v \sin(i)$ , we can estimate a rotation period of 2.4–5.6 hr for 2MASS J1425–36.

4. We combine these new Spitzer detections with the growing sample of young and field brown dwarfs with detected mid-IR variability to investigate their variability amplitudes, inclination angles, and rotation periods, particularly focusing on potential differences between the young and field brown dwarf populations.
5. Previous variability searches found correlations between low gravity and high-amplitude variability for L dwarfs, both in the mid-IR (Metchev et al. 2015) and near-IR (Vos et al. 2019). We find no evidence for an increase in  $3.6 \mu\text{m}$  amplitude in the young dwarfs compared to the field population. At  $4.5 \mu\text{m}$ , we do not find an amplitude enhancement for young, early-L dwarfs. However, there is an apparent enhancement of  $4.5 \mu\text{m}$  amplitude for young, late-L dwarfs.
6. We calculate the inclination angles of each target, finding inclinations of  $22^\circ \pm 1^\circ$  for 2MASS J0045+16,  $60_{-9}^{+20}$  for 2MASS J0501–00, and  $54_{-16}^{+36}$  for 2MASS J1425–36. These new inclination angles are consistent with the tentative relations between inclination, amplitude, and

color reported by Vos et al. (2017). The largest variability amplitudes are observed for brown dwarfs that are observed equator on, and the maximum amplitude decreases for lower inclinations.

7. We find a correlation between inclination angle and  $(J - K)_{2\text{MASS}}$  for the sample of brown dwarfs with measured inclinations. This suggests that brown dwarfs viewed equator on appear redder than the median, and brown dwarfs viewed pole on appear bluer than the median.
8. Finally, we compile the rotation periods of a large sample of brown dwarfs with ages from 1 Myr to field ages, and compare the rotation rates predicted by evolutionary models assuming angular momentum conservation. We find that the rotation rates of the current sample of brown dwarfs generally fall within the limits set by evolutionary models and breakup limits. In future work, we will examine the mass dependence of the spin-up process.

The authors would like to thank the anonymous referee and scientific editor for extensive feedback that significantly improved the clarity of the paper. The authors would like to thank Adam Schneider, Mark Marley, and Alex Scholz for helpful discussions regarding the angular momentum evolution of brown dwarfs; and Jack Gallimore for his contributions to



the DREAM-ZS fitting code. This work is based on observations made with the Spitzer Space Telescope, which is operated by the Jet Propulsion Laboratory, California Institute of Technology, under a contract with NASA. Based on observations obtained at the Gemini Observatory, which is operated by the Association of Universities for Research in Astronomy, Inc., under a cooperative agreement with the NSF on behalf of the Gemini partnership: the National Science Foundation (United States), National Research Council (Canada), CONICYT (Chile), Ministerio de Ciencia, Tecnología e Innovación Productiva (Argentina), Ministério da Ciência, Tecnologia e Inovação (Brazil), and Korea Astronomy and Space Science Institute (Republic of Korea). J.V. acknowledges support by NSF Award Number 1614527 and Spitzer Cycle 14 JPL Research Support Agreement 1627378. T.J.D. is supported by the international Gemini Observatory, a program of NSF's OIR Lab, which is managed by the Association of

Universities for Research in Astronomy (AURA) under a cooperative agreement with the National Science Foundation, on behalf of the Gemini partnership of Argentina, Brazil, Canada, Chile, the Republic of Korea, and the United States of America. T.H. acknowledges support from the European Research Council under the Horizon 2020 Framework Program via the ERC Advanced Grant Origins 83 24 28. The authors wish to recognize and acknowledge the very significant cultural role and reverence that the summit of Maunakea has always had within the indigenous Hawaiian community. We are most fortunate to have the opportunity to conduct observations from this mountain.

## Appendix A Posterior Distributions of Variability Parameters

Figures A1–A3 show the posterior distributions to the MCMC sinusoidal fits discussed in Section 4.3.

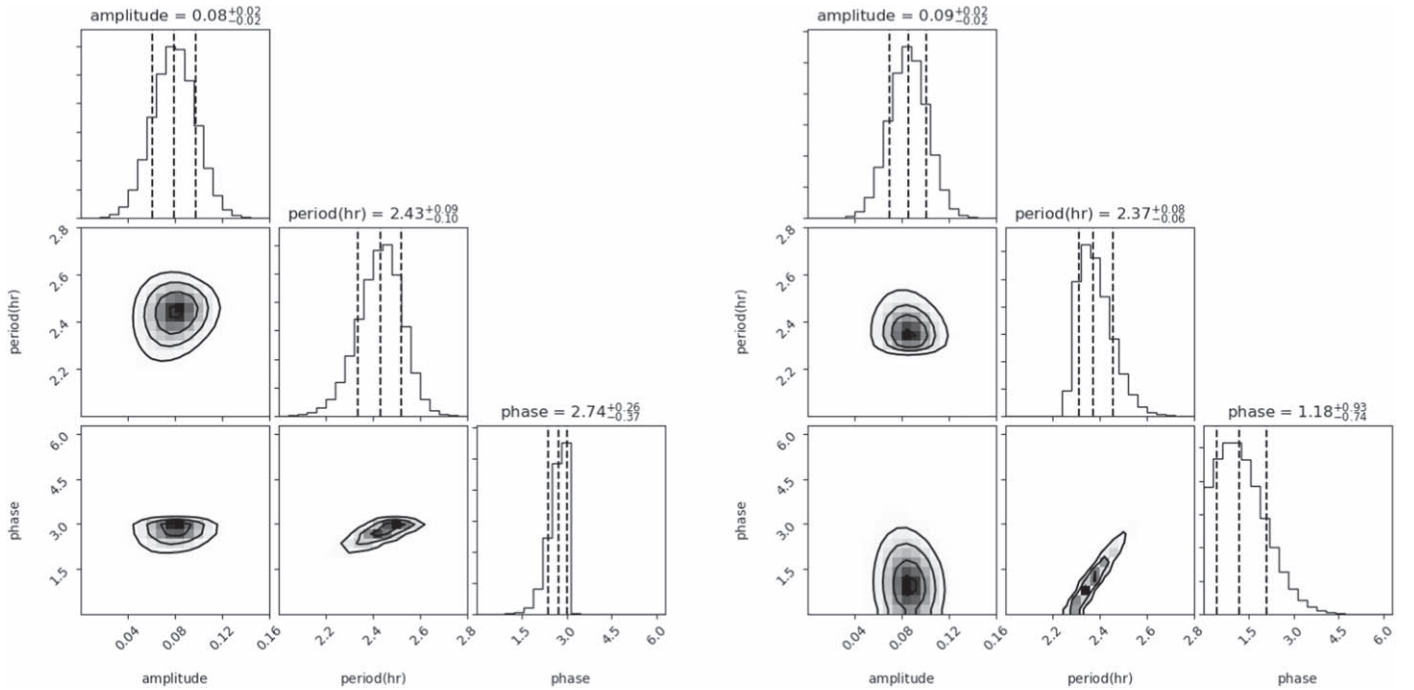


**Figure A1.** Posterior distribution of amplitude, period, and phase parameters for 2MASS J0045+16. Left panel shows parameters for Channel 2 data, right panel shows fit for Channel 1 data.

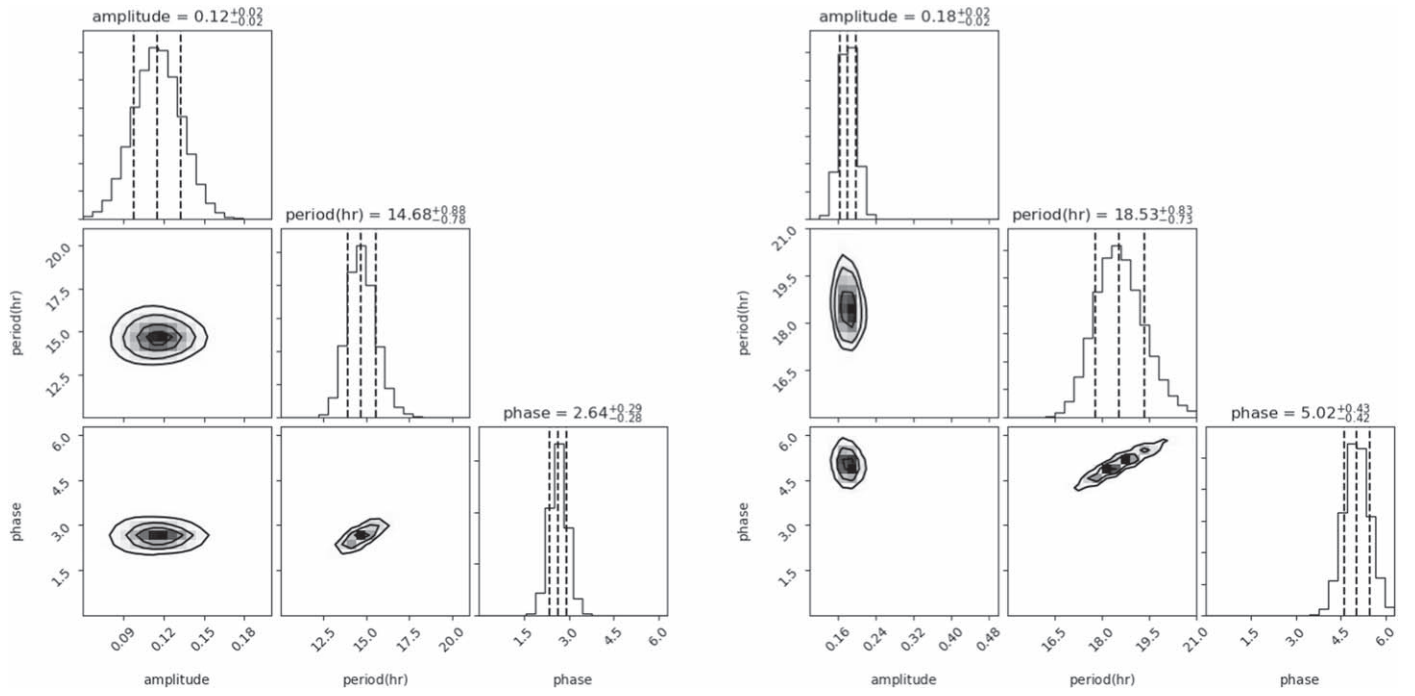


**Figure A2.** Posterior distribution of amplitude, period, and phase parameters for 2MASS J0501–00. Left panel shows parameters for Channel 2 data, right panel shows fit for Channel 1 data.

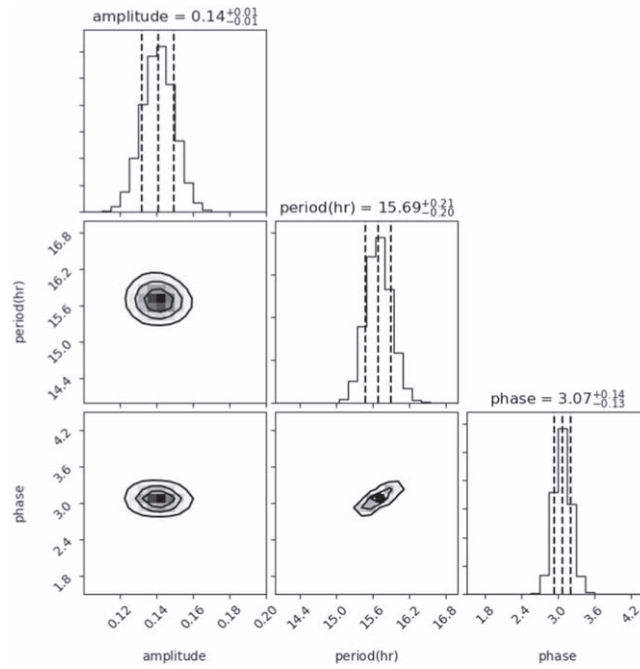


**Figure A3.** Posterior distribution of amplitude, period, and phase parameters for sinusoidal fit to the full Channel 1 and Channel 2 light curves of 2MASS J0501–00.

### Appendix B

#### Pixel Position Variations over Spitzer Variations

Figures B1–B3 show the the corrected Spitzer light curves and the  $(x, y)$  pixel positions over the entire observation for each of our targets. The observed variability is not correlated with the  $(x, y)$  pixel position.

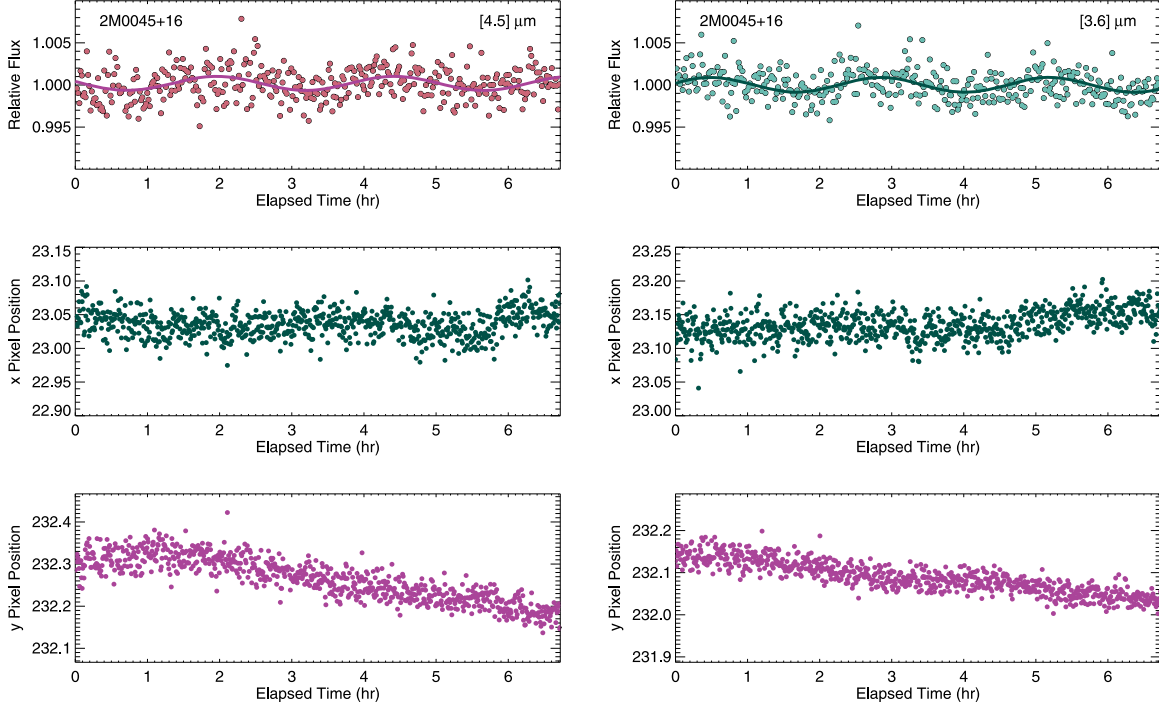


**Figure B1.** Corrected relative flux (top panel), x-pixel position (middle panel), and y-pixel position (bottom panel) for Spitzer [4.5  $\mu\text{m}$ ] (left) and [3.6  $\mu\text{m}$ ] (right) monitoring of 2MASS J0045+16. The observed variability is not correlated with the  $(x, y)$  pixel positions.

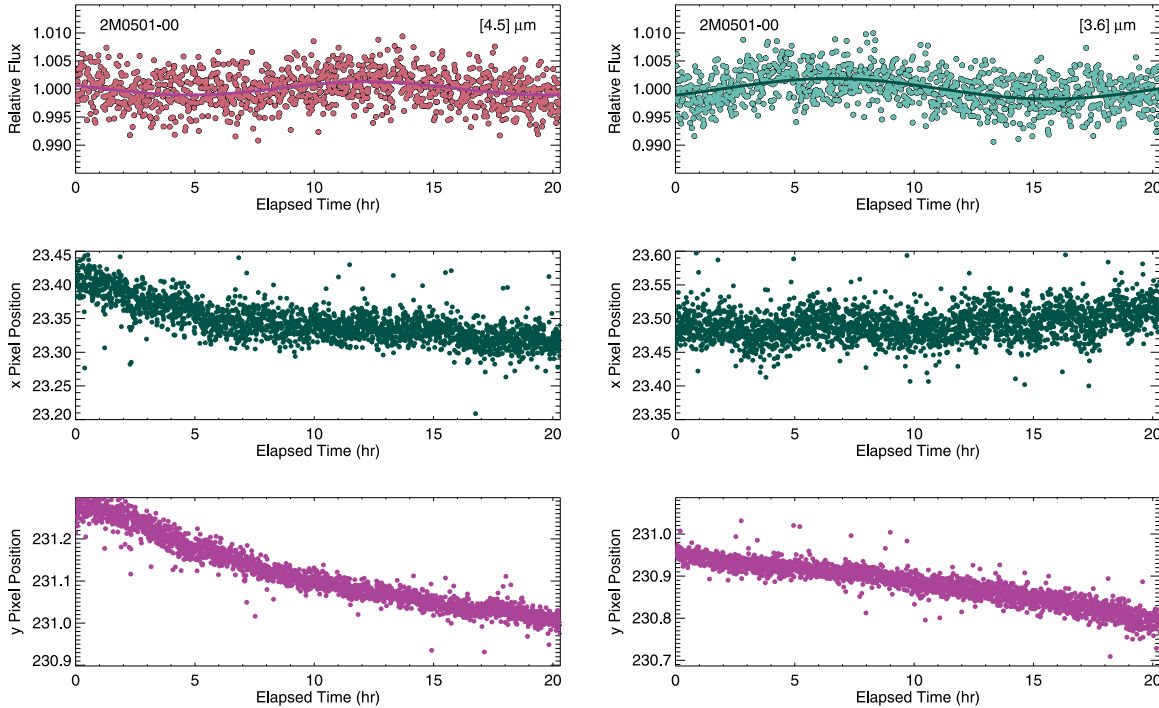


**Figure B2.** Corrected relative flux (top panel), x-pixel position (middle panel), and y-pixel position (bottom panel) for Spitzer [4.5  $\mu\text{m}$ ] (left) and [3.6  $\mu\text{m}$ ] (right) monitoring of 2MASS J0501-00. The observed variability is not correlated with the  $(x, y)$  pixel positions.

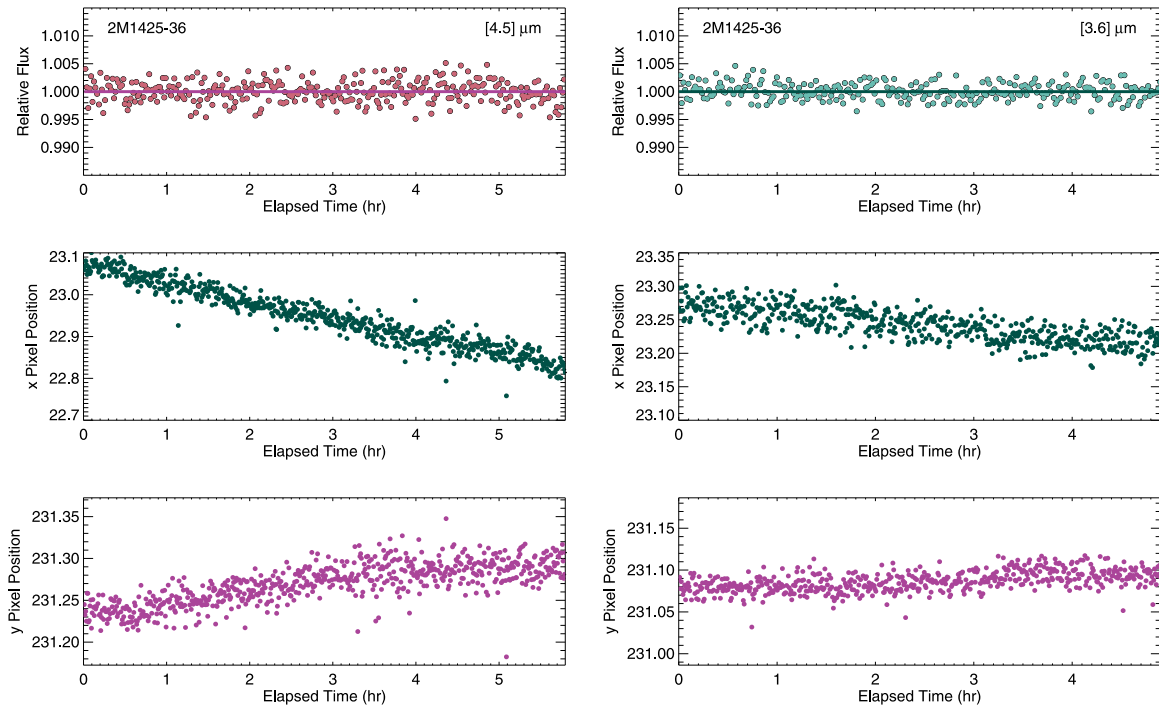


**Figure B3.** Corrected relative flux (top panel), x-pixel position (middle panel), and y-pixel position (bottom panel) for Spitzer [4.5  $\mu\text{m}$ ] (left) and [3.6  $\mu\text{m}$ ] (right) monitoring of 2MASS J1425–36. We do not detect significant variability in 2MASS J1425–36.

### ORCID iDs

Johanna M. Vos <https://orcid.org/0000-0003-0489-1528>  
 Beth A. Biller <https://orcid.org/0000-0003-4614-7035>  
 Katelyn N. Allers <https://orcid.org/0000-0003-0580-7244>  
 Jacqueline K. Faherty <https://orcid.org/0000-0001-6251-0573>  
 Michael C. Liu <https://orcid.org/0000-0003-2232-7664>  
 Stanimir Metchev <https://orcid.org/0000-0003-3050-8203>  
 Elena Manjavacas <https://orcid.org/0000-0003-0192-6887>  
 Trent J. Dupuy <https://orcid.org/0000-0001-9823-1445>  
 Markus Janson <https://orcid.org/0000-0001-8345-593X>  
 William M. J. Best <https://orcid.org/0000-0003-0562-1511>  
 Derek Homeier <https://orcid.org/0000-0002-8546-9128>  
 Joshua E. Schlieder <https://orcid.org/0000-0001-5347-7062>  
 Mariangela Bonavita <https://orcid.org/0000-0002-7520-8389>  
 Esther Buenzli <https://orcid.org/0000-0003-3306-1486>

### References

- Allard, F., Homeier, D., & Freytag, B. 2012, *RSPTA*, 370, 2765  
 Allers, K. N., Gallimore, J. F., Liu, M. C., & Dupuy, T. J. 2016, *ApJ*, 819, 133  
 Allers, K. N., & Liu, M. C. 2013, *ApJ*, 772, 79  
 Allers, K. N., Vos, J. M., Biller, B. A., & Williams, P. K. G. 2020, *Sci*, 368, 169  
 Apai, D., Karalidi, T., Marley, M. S., et al. 2017, *Sci*, 357, 683  
 Apai, D., Kasper, M., Skemer, A., et al. 2016, *ApJ*, 820, 40  
 Artigau, É 2018, in *Handbook of Exoplanets*, ed. H. Deeg & J. Belmonte (Cham: Springer), 555  
 Baraffe, I., Homeier, D., Allard, F., & Chabrier, G. 2015, *A&A*, 577, A42  
 Best, W. M. J., Liu, M. C., Dupuy, T. J., & Magnier, E. A. 2017, *ApJL*, 843, L4  
 Biller, B. 2017, *AstRv*, 2857, 1  
 Biller, B. A., Vos, J., Bonavita, M., et al. 2015, *ApJL*, 813, L23  
 Biller, B. A., Vos, J., Buenzli, E., et al. 2018, *AJ*, 155, 95  
 Blake, C. H., Charbonneau, D., & White, R. J. 2010, *ApJ*, 723, 684  
 Bouchy, F., Hebb, L., Skillen, I., et al. 2010, *A&A*, 519, A98  
 Bouvier, J., Matt, S. P., Mohanty, S., et al. 2014, in *Protostars and Planets VI*, ed. H. Beuther et al. (Tucson, AZ: Univ. Arizona Press)  
 Bowler, B. P., Zhou, Y., Morley, C. V., et al. 2020, *ApJL*, 893, L30  
 Buenzli, E., Apai, D., Morley, C. V., et al. 2012, *ApJL*, 760, L31  
 Buenzli, E., Apai, D., Radigan, J., Reid, I. N., & Plateau, D. 2014, *ApJ*, 782, 77  
 Buenzli, E., Saumon, D., Marley, M. S., et al. 2015, *ApJ*, 798, 127  
 Chabrier, G., Baraffe, I., Allard, F., & Hauschildt, P. 2000, *ApJ*, 542, 464  
 Clarke, F. J., Hodgkin, S. T., Oppenheimer, B. R., Robertson, J., & Haubois, X. 2008, *MNRAS*, 386, 2009  
 Cody, A. M., & Hillenbrand, L. A. 2010, *ApJS*, 191, 389  
 Croll, B., Muirhead, P. S., Han, E., et al. 2016, arXiv:1609.03586  
 Cruz, K. L., Kirkpatrick, J. D., & Burgasser, A. J. 2009, *AJ*, 137, 3345  
 Cushing, M. C., Hardegree-Ullman, K. K., Trucks, J. L., et al. 2016, *ApJ*, 823, 152  
 Deleuil, M., Deeg, H. J., Alonso, R., et al. 2008, *A&A*, 491, 889  
 Delrez, L., Gillon, M., Triard, A. H. M. J., et al. 2018, *MNRAS*, 475, 3577  
 Dupuy, T. J., & Liu, M. C. 2012, *ApJS*, 201, 19  
 Eriksson, S., Janson, M., & Calissendorff, P. 2019, *A&A*, 629, A145  
 Esplin, T. L., Luhman, K. L., Cushing, M. C., et al. 2016, *ApJ*, 832, 58  
 Faherty, J. K., Riedel, A. R., Cruz, K. L., et al. 2016, *ApJS*, 225, 1  
 Fasano, G., & Franceschini, A. 1987, *MNRAS*, 225, 155  
 Fazio, G. G., Hora, J. L., Allen, L. E., et al. 2004, *ApJS*, 154, 10  
 Filippazzo, J. C., Rice, E. L., Faherty, J., et al. 2015, *ApJ*, 810, 158  
 Foreman-Mackey, D., Hogg, D. W., Lang, D., & Goodman, J. 2013, *PASP*, 125, 306  
 Gagné, J., Faherty, J. K., Burgasser, A. J., et al. 2017, *ApJL*, 841, L1  
 Gagné, J., Faherty, J. K., Cruz, K. L., et al. 2015, *ApJS*, 219, 33  
 Gillon, M., Triard, A. H. M. J., Jehin, E., et al. 2013, *A&A*, 555, L5  
 Girardin, F., Artigau, É., & Doyon, R. 2013, *ApJ*, 767, 61  
 Gizis, J. E., Faherty, J. K., Liu, M. C., et al. 2012, *AJ*, 144, 94  
 Heinze, A. N., Metchev, S., Apai, D., et al. 2013, *ApJ*, 767, 173  
 Heinze, A. N., Metchev, S., & Kellogg, K. 2015, *ApJ*, 801, 104  
 Hiranaka, K., Cruz, K. L., Douglas, S. T., Marley, M. S., & Baldassare, V. F. 2016, *ApJ*, 830, 96  
 Knutson, H. A., Charbonneau, D., Allen, L. E., Burrows, A., & Megeath, S. T. 2008, *ApJ*, 673, 526  
 Leggett, S. K., Cushing, M. C., Hardegree-Ullman, K. K., et al. 2016, *ApJ*, 830, 141  
 Lew, B. W. P., Apai, D., Zhou, Y., et al. 2016, *ApJL*, 829, L32  
 Littlefair, S. P., Casewell, S. L., Parsons, S. G., et al. 2014, *MNRAS*, 445, 2106  
 Liu, M. C., Dupuy, T. J., & Allers, K. N. 2016, *ApJ*, 833, 96  
 Liu, M. C., Magnier, E. A., Deacon, N. R., et al. 2013, *ApJL*, 777, L20  
 Manjavacas, E., Apai, D., Lew, B. W. P., et al. 2019, *ApJL*, 875, L15



- Manjavacas, E., Apai, D., Zhou, Y., et al. 2018, [AJ](#), **155**, 11
- Marley, M. S., Saumon, D., Cushing, M., et al. 2012, [ApJ](#), **754**, 135
- Metchev, S. A., Heinze, A., Apai, D., et al. 2015, [ApJ](#), **799**, 154
- Miles-Pérez, P. A., Metchev, S., Apai, D., et al. 2019, [ApJ](#), **883**, 181
- Moore, K., Scholz, A., & Jayawardhana, R. 2019, [ApJ](#), **872**, 159
- Morales-Calderón, M., Stauffer, J. R., Kirkpatrick, J. D., et al. 2006, [ApJ](#), **653**, 1454
- Naud, M.-E., Artigau, É., Doyon, R., et al. 2017, [AJ](#), **154**, 129
- Peacock, J. A. 1983, [MNRAS](#), **202**, 615
- Pont, F., Melo, C. H. F., Bouchy, F., et al. 2005, [A&A](#), **433**, L21
- Press, W. H., Flannery, B. P., & Teukolsky, S. A. 1986, Numerical Recipes. The Art of Scientific Computing (Cambridge: Cambridge Univ. Press)
- Radigan, J., Jayawardhana, R., Lafrenière, D., et al. 2012, [ApJ](#), **750**, 105
- Radigan, J., Lafrenière, D., Jayawardhana, R., & Artigau, E. 2014, [ApJ](#), **793**, 75
- Riedel, A. R., Blunt, S. C., Lambrides, E. L., et al. 2017, [AJ](#), **153**, 95
- Riedel, A. R., DiTomaso, V., Rice, E. L., et al. 2019, [AJ](#), **157**, 247
- Rodríguez-Ledesma, M. V., Mundt, R., & Eislöffel, J. 2009, [A&A](#), **502**, 883
- Saumon, D., & Marley, M. 2008, [ApJ](#), **689**, 1327
- Scargle, J. D. 1982, [ApJ](#), **263**, 835
- Schneider, A. C., Hardegree-Ullman, K. K., Cushing, M. C., Kirkpatrick, J. D., & Shkolnik, E. L. 2018, [AJ](#), **155**, 238
- Scholz, A., & Eislöffel, J. 2004, [A&A](#), **419**, 249
- Scholz, A., & Eislöffel, J. 2005, [A&A](#), **429**, 1007
- Scholz, A., Kostov, V., Jayawardhana, R., & Mužić, K. 2015, [ApJL](#), **809**, L29
- Scholz, A., Moore, K., Jayawardhana, R., et al. 2018, [ApJ](#), **859**, 153
- Schwarz, G. 1978, [AnSta](#), **6**, 461
- Showman, A. P., Tan, X., & Zhang, X. 2019, [ApJ](#), **883**, 4
- Siverd, R. J., Beatty, T. G., Pepper, J., et al. 2012, [ApJ](#), **761**, 123
- Tremblin, P., Amundsen, D. S., Chabrier, G., et al. 2016, [ApJL](#), **817**, L19
- Vos, J. M., Allers, K. N., & Biller, B. A. 2017, [ApJ](#), **842**, 78
- Vos, J. M., Allers, K. N., Biller, B. A., et al. 2018, [MNRAS](#), **474**, 1041
- Vos, J. M., Biller, B. A., Bonavita, M., et al. 2019, [MNRAS](#), **483**, 480
- Yang, H., Apai, D., Marley, M. S., et al. 2016, [ApJ](#), **826**, 8
- Zhou, Y., Apai, D., Lew, B. W. P., et al. 2019, [AJ](#), **157**, 128
- Zhou, Y., Apai, D., Metchev, S., et al. 2018, [AJ](#), **155**, 132
- Zhou, Y., Apai, D., Schneider, G. H., Marley, M. S., & Showman, A. P. 2016, [ApJ](#), **818**, 176
- Zhou, Y., Bowler, B. P., Morley, C. V., et al. 2020, arXiv:2004.05168